Tracking Sediment Transport Through Miage Glacier, Italy, Using a Lagrangian Approach With Luminescence Rock Surface Burial Dating of Englacial Clasts

Audrey Margirier[1,2] , **Julien Brondex[1,3]** , **Ann V. Rowan[4]** , **Christoph Schmidt[1]**, **Vivi K. Pedersen[5]** , **Benjamin Lehmann[2]**, **Leif S. Anderson[1,6]** , **Remy Veness[7]** , **C. Scott Watson[8]** , **Darrel Swift[9]**, and **Georgina E. King[1]**

[1]Institute of Earth Surface Dynamics, University of Lausanne, Lausanne, Switzerland, [2]Université Grenoble Alpes, Université Savoie Mont Blanc, CNRS, IRD, IFSTTAR, ISTerre, Grenoble, France, [3]Université Grenoble Alpes, IRD, CNRS, Grenoble INP, IGE, Grenoble, France, [4]Department of Earth Science, University of Bergen and Bjerknes Centre for Climate Research, Bergen, Norway, [5]Department of Geoscience, Aarhus University, Aarhus C, Denmark, [6]Department of Geology and Geophysics, University of Utah, Salt Lake City, UT, USA, [7]Department of the Natural and Built Environment, Sheffield Hallam University, Sheffield, UK, [8]School of Geography, University of Leeds, Leeds, UK, [9]Department of Geography, University of Sheffield, Sheffield, UK

Abstract Constraining the timescales of sediment transport by glacier systems is important for understanding the processes controlling sediment dynamics within glacierized catchments, and because the accumulation of supraglacial sediment influences glacier response to climate change. However, glacial sediment transport can be difficult to observe; sediment can be transported englacially, subglacially, supraglacially or at the ice margins, and may be stored temporarily on headwall slopes or within moraines before being (re-)entrained and transported by glacier ice. This study is a proof of concept of the use of luminescence rock surface burial dating to establish rates of englacial sediment transport. Our novel approach combines luminescence rock surface burial dating of englacial clasts with an ice-flow model that includes Lagrangian particle tracking to quantify rates of sediment transport through the Miage Glacier catchment in the Italian Alps. Luminescence rock surface burial ages for seven samples embedded in the near-surface ice in the ablation area range from 0.0 ± 1.0 to 4.7 ± 0.3 ka and are consistent with the ice-flow model results. Our results show that the transport durations of individual clasts vary by an order of magnitude, implying rapid clast transport near the glacier surface and longer transport histories for clasts transported lower in the ice column. In some cases, clasts were stored on the headwalls or within ice-marginal moraines for several thousand years before being englacially transported. The results illustrate the different routes by which glaciers transport sediment and provide the first direct measurements of englacial sediment transport duration.

Plain Language Summary Constraining how sediment moves through glacier catchments is crucial for understanding glacier dynamics and landscape evolution. However, glacial sediment transport processes are challenging to observe directly; sediment can be transported englacially, subglacially, supraglacially or along the ice margins, and may be deposited before being re-entrained within glacier ice. We developed a new method combining luminescence rock surface burial dating with a Lagrangian glacier model to investigate Holocene (∼12 ka to present day) sediment transport histories through Miage Glacier in the Italian Alps. Luminescence measurements constrain sediment burial since the last sunlight exposure. Luminescence rock surface burial ages for seven clasts collected from the glacier ablation area range from 0.0 ± 1.0 to 4.7 ± 0.3 ka and are consistent with the simulated transport durations. The glacier model results indicate that sediment transport durations vary depending on the route taken, with sediments transported near the ice surface moving through the glacier an order of magnitude more rapidly than those transported lower in the ice column. Moreover, some sediment is stored on headwalls or in moraines for thousands of years before (further) glacier transport.

1. Introduction

Understanding of the flow of ice through rugged mountain topography has developed from early experimental and numerical studies of ice physics and ice flow through low-aspect ratio ice sheets to accurately represent the dynamics of mountain glaciers (Egholm et al., 2011; Glen, 1955; Zekollari et al., 2022). Glaciers transport

Project administration: Georgina E. King

Resources: Christoph Schmidt, Georgina E. King

Supervision: Christoph Schmidt, Georgina E. King

Visualization: Audrey Margirier, Ann V. Rowan

Writing – original draft: Audrey Margirier, Ann V. Rowan, Georgina E. King

Writing – review & editing: Audrey Margirier, Julien Brondex, Ann V. Rowan, Christoph Schmidt, Vivi K. Pedersen, Benjamin Lehmann, Leif S. Anderson, Remy Veness, C. Scott Watson, Darrel Swift, Georgina E. King

sediment as well as ice, which can substantially affect their evolution (e.g., Benn & Lehmkuhl, 2000; Lane et al., 2017) and create distinctive erosional and depositional landforms (e.g., Ivy-Ochs et al., 2009; Mackintosh et al., 2017; Pedersen & Egholm, 2013). However, the time scales and pathways of sediment transport through glacial catchments are difficult to observe and relatively poorly understood. In the case of englacial transport of sediment, all grain sizes incorporated in the ice move together, meaning that the transport rates of both fine grains and large clasts should be similar. Englacial sediment transport may be influenced by englacial structures such as fractures, thrusts, and foliations, the sediment input location, and the internal 3-D ice velocity field (Iverson, 1993; Jennings & Hambrey, 2021). Sediment produced by subglacial erosion and incorporated into the lower part of the ice column either remains close to the glacier bed or may be moved upwards via the incorporation of sediment into longitudinal or transverse foliation or brittle thrusting (Fushimi, 1977; Hambrey et al., 1999; Hubbard & Sharp, 1995). The dynamic state of a glacier in terms of its mass balance and the basal thermal regime will therefore determine when and where sediment is entrained into or deposited from flowing ice (Delaney & Adhikari, 2020; Iverson, 1993). Constraining the pathways and time scales of glacial sediment transport is of interest for understanding the processes that move sediment through glacierized catchments and the impacts of sediment transport on glacier evolution. However, two main challenges remain: (a) there is a lack of established methods to quantify englacial sediment transport, and (b) numerical models of ice flow often rely on approximations that consider specific components of the stress tensor being negligible. On the other hand, computed ice flow trajectories may not (completely) account for the storage of sediment at the glacier margins.

For valley glaciers, englacial sediment is most often derived from rock avalanching into the accumulation area from adjacent hillslopes. Sediment is then incorporated into the ice and transported englacially until it melts out at the ice surface in the ablation area. Melt-out debris, together with debris deposited by rockfalls directly onto the ablation area, predominantly remains at the ice surface as it is conveyed down glacier (Anderson, 2000; Kirkbride & Deline, 2013; Rowan et al., 2015). Debris-covered glaciers, which represent about 7% of the current global glacial area, are those that exhibit particularly thick and extensive surface "debris" layer. This glacier type is becoming more common as glacier mass loss causes supraglacial debris mantles to expand and thicken (Herreid & Pellicciotti, 2020). The accumulation of supraglacial debris can reduce ablation by insulating the ice surface (e.g., Lejeune et al., 2013; Nicholson & Benn, 2006), allowing a glacier to expand beyond the limits of a clean-ice glacier under equivalent climatic conditions (Anderson et al., 2018). When a glacier is close to dynamic equilibrium, supraglacial debris is efficiently exported to the ice margins and deposited to form lateral and terminal moraines (Rowan et al., 2015). However, during deglaciation, extensive supraglacial debris layers may develop because ice flux reduces and headwall areas expand and destabilize (Fyffe et al., 2020; Scherler et al., 2018). The accumulation of debris on glacier surfaces is therefore related to climate change, as headwall erosion, glacier mass balance, and ice flow are sensitive to mean annual air temperature (Deline, 2009; Hales & Roering, 2009; Scherler, 2014). The timing of the initial formation and the rate of expansion of supraglacial debris mantles varies depending on catchment geometry and bedrock lithology, with glaciers that are subjected to frequent or high-magnitude rock avalanches tending to develop a debris mantle earlier than those dominated by exhumation of englacial debris (Deline, 2005).

Ice can take hundreds to thousands of years to flow through a large glacier (Jouvet et al., 2020; Zekollari et al., 2022). While the tracking of surface features such as supraglacial boulders using satellite imagery is routinely used to produce maps of glacier surface velocities worldwide (e.g., Dehecq et al., 2019; Millan et al., 2022; Quincey et al., 2009), the velocity field below the glacier surface is notably more difficult to observe and often remains unconstrained (Jennings & Hambrey, 2021; Miles et al., 2022). A few previous studies have used the bodies of mountaineers or fragments of aircraft trapped on glacier surfaces and encapsulated within ice to identify the point where these were deposited onto the glacier (Compagno et al., 2019; Jouvet & Funk, 2014). Radionuclides of known ages collected from a glacier surface have also been used as tracers to develop an understanding of englacial flow (Jouvet et al., 2020). The discovery of a 5.3 ka Neolithic mummy in the ice of the Fineilspitze in the Ötztal Alps (Bonani et al., 1994) illustrates that in specific cases, material can be stored for thousands of years in stagnant ice patches (i.e., ice-filled hollows). Cold-based ice aprons on steep slopes could store rock debris for thousands of years that may later be released into englacial transport (e.g., Ravanel et al., 2023). For example, basal ice from the Col du Dôme in the Miage Glacier catchment has been dated to ~5 ka (Preunkert et al., 2019) and the horizontal rate of ice flow close to the margin is less than 5 m a^{-1} (Vincent et al., 2020).

Using the Miage Glacier in the Italian Alps on the southern side of the Mont Blanc massif as a test-case, we apply a novel approach that combines luminescence rock surface burial dating with ice-flow model experiments to

quantify the duration and pathways of sediment transport through a glacierized alpine catchment. Luminescence rock surface burial dating is a precise geochronological method to measure the duration of a period (or multiple periods) of rock burial (e.g., Chapot et al., 2012; Freiesleben et al., 2015; Jenkins et al., 2018; Sohbati et al., 2011) and can therefore identify how long a rock clast is stored or transported within a glacier. To evaluate and interpret the luminescence ages, we used a particle-tracking algorithm implemented within a higher-order ice-dynamical glacier evolution model (Scherler & Egholm, 2020) to simulate the transport pathways of sediment produced by headwall erosion. We then compared the total transport and storage time of each simulated particle in the glacier model to the luminescence rock surface burial ages, as both reflect the duration the clast spent being transported within or beneath the glacier after its erosion. This new approach promises to increase understanding of Holocene (~12 ka to present day) sediment transport dynamics within englaciated mountain catchments. In the model experiments, sediment in contact with the glacier was simulated as Lagrangian particles that were tracked through the ice over time. The term "particle" throughout this manuscript exclusively refers to the simulated englacial sediment particles within the model. This allows for a comparison between the luminescence rock surface burial ages with the integrated transport and storage time represented by each particle in the glacier model. Due to the technical requirement of rock surface burial dating, which involves coring the clast, we focused on englacial rock clasts thicker than 6 cm.

2. Miage Glacier, Italy

Miage Glacier (RGI60–11.03005; Figure 1) is a debris-covered glacier that is 10.5 km in length, ranging in elevation from 1,736 to 4,776 m above sea level (RGI Consortium, 2017) that descends from the Mont Blanc Massif to the Aosta Valley, Italy. The glacier area was estimated as 9.3 km^2 in 2021 (Stefaniak et al., 2021). The glacier has a bifurcated terminus with two large and one small debris-covered tongues surrounded by Holocene ice-marginal moraines from which only minor recession has occurred between the Little Ice Age and the present day (Deline, 2005; Kirkbride, 2000). Mean annual centerline velocities through the main tongue of Miage Glacier of up to 80 m a^{-1} were observed between 1975 and 1991 from tracking of supraglacial boulders (Smiraglia et al., 2000). Mean annual glacier-wide surface velocities determined using feature tracking were 35 ± 0.1 m a^{-1} in 1990–1991 and reduced by 46% to 16 ± 0.1 m a^{-1} in 2017–2018, while surface velocity in the terminal lobes decreased by 70% to 6.0 ± 0.1 m a^{-1} over the same period (Stefaniak et al., 2021).

The debris mantle initiated near the terminus at around 1850 CE and expanded to reach its present-day extent in the 1930s (Deline, 2005). Supraglacial debris currently covers about 5 km^2 of the ablation area and ranges in thickness from 0.05 to 0.30 m, increasing up to 1.0 m on the terminal lobes (Foster et al., 2012; Stefaniak et al., 2021; Thomson et al., 2000). As the area mantled by supraglacial debris increased, Miage Glacier increased in volume during the 20th Century despite increasing mean annual air temperatures that caused a century-averaged volume loss from equivalent clean-ice glaciers (Thomson et al., 2000). However, the rate of expansion of Miage Glacier slowed toward the end of the 20th Century, and, in common with debris-covered glaciers worldwide, the long-term (centennial) insulating effect of supraglacial debris mantles is now overturned by the widespread impact of rapid climate warming and differential ablation processes (e.g., the formation and expansion of supraglacial ice cliffs and ponds) (Buri et al., 2021; Pellicciotti et al., 2015; Rowan et al., 2021; Thomson et al., 2000). Widespread mass loss from Miage Glacier since 1990 is indicated by an 11% reduction in glacier area and about 50 m of terminus recession; however, the rate of surface change declined from -1.07 ± 0.10 m a^{-1} between 1990 and 2008 to -0.85 ± 0.01 m a^{-1} between 2008 and 2018, which is attributed to the expansion of the debris mantle and the associated reduction in sub-debris melt (Stefaniak et al., 2021).

3. Methods

3.1. Luminescence Rock Surface Burial Dating

We used luminescence rock surface burial dating (Sohbati et al., 2011) to constrain the englacial transport time of rock debris within the Miage Glacier. In contrast to classical luminescence dating that is usually applied to sand-sized grains of quartz and feldspar, rock surface burial dating is applied to larger pebble or cobble sized clasts or rock surfaces. This method provides a key advantage by allowing the assessment of complete bleaching of the luminescence signal in the targeted samples, which is a frequent challenge in traditional luminescence dating of sediments in glacial environments (e.g., Fuchs & Owen, 2008; Prescott & Robertson, 1997). In its simplest form, the luminescence signal of the buried clast surface is measured to determine the burial age of the clast, i.e., the
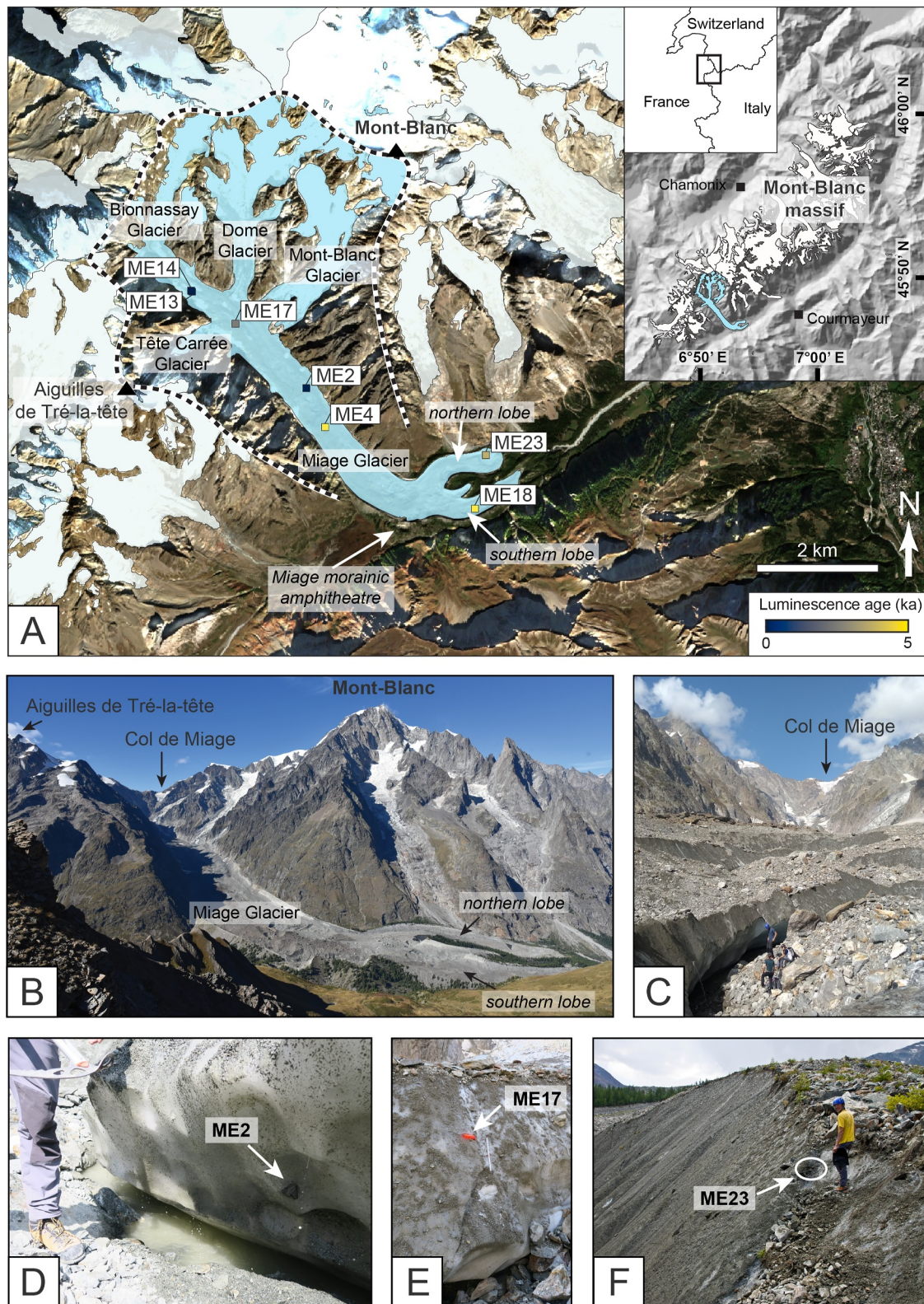
Figure 1. (a) Location of the study area. Aerial image of the Miage Glacier (in blue) showing the glaciated area, the limits of the Miage Glacier catchment (highlighted with the dashed line) and sample locations. The symbol color indicates the minimum luminescence age of the sample. The inset shows the location of the Miage Glacier within the Mont-Blanc Massif and at a regional scale. (b) Photograph of the Miage Glacier. (c) Photograph of the debris cover on the glacier surface. (d)–(f) Photographs of sampling sites and rock debris embedded in the ice just before sampling.
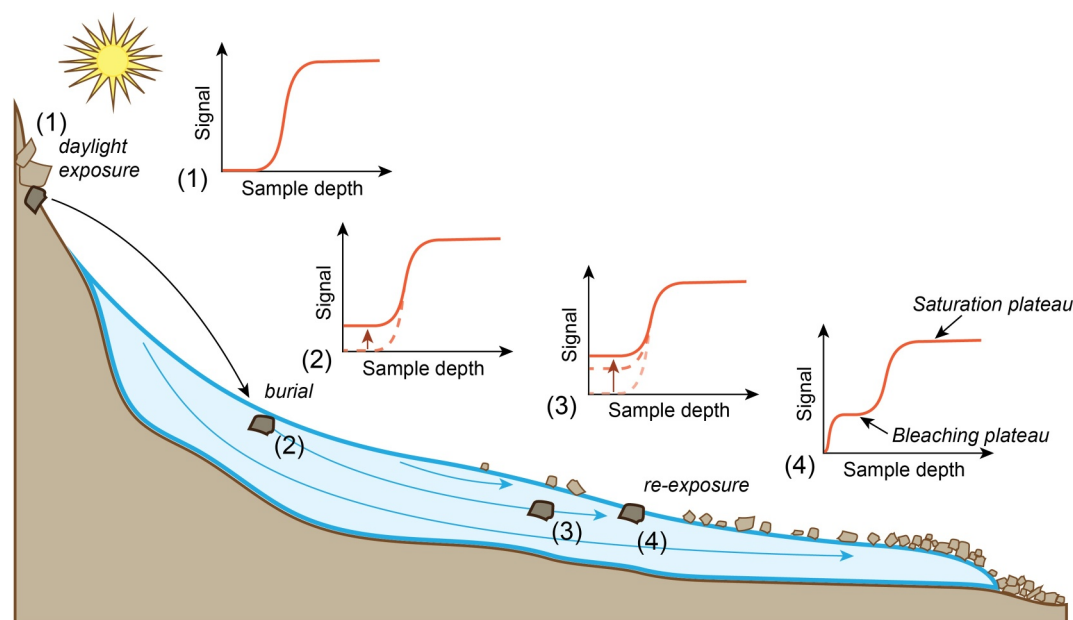
Figure 2. Schematic view of englacial debris transport and expected luminescence signal. The luminescence signal is bleached at the surface of the rock during its exposure to natural light on the headwalls (1). After the rock debris falls on the glacier when it is buried in the ice, the luminescence signal starts increasing (2). During the whole duration of the englacial history, the luminescence signal increases (3). If the rock debris is exposed to light when emerging from the ice in the ablation zone, the luminescence signal is bleached at the surface (4).

time since the clast surface was last exposed to sunlight. Rock surface burial dating has recently been used in glaciofluvial (Jenkins et al., 2018; Serra et al., 2025) and paraglacial environments (Rades et al., 2018) but has not yet been applied to constrain the burial duration of englacial sediment. The successful application of luminescence rock surface burial dating to constrain the burial duration of rock debris within the ice requires that (a) the luminescence signal was bleached within at least the first few millimeters of the surface of the rock prior to burial and (b) that the ice shields the rock surface from sunlight after burial (Figure 2). In the Miage Glacier, the ice contains a lot of dirt and debris, and the ice likely shields rock clasts from sunlight within a maximum of a few years. When the rock is shielded from sunlight, the luminescence signal starts to accumulate such that a longer burial duration corresponds to a higher luminescence signal of the bleaching plateau (Figure 2).

3.1.1. Sample Collection and Preparation

Samples were collected from 14 sites in the ablation area of Miage Glacier (Figure 1; Table S1 in Supporting Information S1). The samples were collected in the upper part of the ice column, away from the glacier margins to prevent the sampling of rock clasts re-entrained from the ice-marginal moraines. We sampled 24 rock clasts embedded in the ice or partially emerging from ice cliffs, presumed to have entered glacial transport in the accumulation area of the glacier. Where the sample was emerging from the ice, we marked the uppermost surface that was exposed to sunlight. After collection, each sample was packed in a light-tight black bag to avoid additional light exposure. The samples were angular with diameters ranging from 6 to 24 cm. None of the rock clasts had visible striations, suggesting a rockfall origin and exclusively englacial transport. Samples comprised a variety of different lithologies including schist, gneiss, and felsic intrusive rocks. 18 samples were processed for luminescence rock surface burial dating after successful coring. Sample preparation and measurement were carried out in the luminescence laboratory at the University of Lausanne. Cores of 10 mm in diameter were taken from the buried parts of the rock samples and sliced using a Buehler Isomet high precision saw into discs ~0.7 mm thick. We cored the largest available clast faces and measured the thickness of each rock slice to determine the rock slice depth from the clast surface, accounting for the thickness of the sawing blade. A portion of each sample was also sent for ICP-MS analysis at Activation Laboratories Canada for environmental dose rate determination.

3.1.2. Luminescence Measurements

The luminescence signals were measured using DASH-equipped Risø TL/OSL DA20 luminescence readers following the protocol of Elkadi et al. (2021). Fragments of each rock slice were placed in stainless steel cups for measurement. The natural luminescence signal (L_n) was measured from the surface to a maximum depth of 9–17 mm using a protocol comprising a 250°C preheat for 60 s and then infrared stimulation at 50°C (IRSL$_{50}$), post-infrared infrared stimulated luminescence at 225°C (post-IR IRSL$_{225}$) and blue stimulation at 125°C (OSL$_{125}$). Infrared stimulated luminescence measurements were detected using the blue filter pack (Schott BG39+BG3) whilst OSL measurements were detected in the UV using a 7.5 mm Hoya U340 filter. A heating rate of 1°C s^{-1} was used for all measurements and a 100 s pause was included prior to optical stimulation of the samples for 200 s. Infrared stimulated luminescence signals were integrated for the first 12.5 s and background signals were integrated for the last 50 s. The OSL signal was integrated over 4.2 s and the corresponding background over the last 50 s. Test doses of 33.6 and 42.7 Gy were used to normalize the luminescence signal of every rock slice dependent on the instrument. The built-in β-sources were calibrated with 0.7 mm thick quartzite slices γ-irradiated at the Institute of Radiation Physics of the University Hospital Lausanne (CHUV), yielding dose rates in the range 0.13–0.16 Gy s^{-1}. No samples were discarded due to low signal intensity (i.e., all measurements yielded signals >3σ above the background signal).

To confirm that luminescence signals had been sufficiently bleached at the rock surface before being buried in the ice, and thus that they were suitable for constraining the samples' burial duration, we followed the approach of al Khasawneh et al. (2019). We constructed luminescence depth profiles for each of the samples by measuring the natural luminescence of fragments of each disc from each core, and then fitted these data using the model of Freiesleben et al. (2015) to estimate the burial duration (t_b) and bleaching duration (t) (Figures 3a–3c, see complete information on the model in the Supporting Information S1). Surface slices were weighted to ensure a satisfactory fit of the data in the surficial part of the core. For each core, the natural luminescence signal depth profile (L_{bur}, solid line in Figures 3a–3c) was then compared to a modeled pre-burial luminescence signal exposure (bleaching) profile (L_{exp}, dashed line in Figures 3a–3c), following al Khasawneh et al. (2019). We applied a threshold of >5% difference between the measured luminescence signals and the modeled exposure profile, L_{exp} (green shaded zone in the inset of Figures 3a–3c); if at least the two first rock slice fragments show a pre-burial signal <5% of the measured burial signal, we retained the core. A depth-dependent dose rate could theoretically affect this test; however, the variation in dose rates within the first 2 mm from the surface of the clast is negligible (see Section 3.1.3 for details). In addition, we excluded samples where the luminescence signal of the surface slices was within 3σ error of the saturation plateau (Figure 2). This allows samples with surface slices that are saturated or close to saturation to be excluded.

Equivalent dose (D_e) values were determined for all the slices that passed the plateau test using new fragments for construction of the dose-response curve (Figure 3d). To construct the dose-response curve, the same protocol was used for measurement of the natural luminescence signal but including multiple cycles with regenerative doses up to 3,859 Gy. All dose-response curves fulfilled the acceptance criteria of a recycling ratio <10%, L_n >3σ above background and recuperation <5%. Dose response curves were fitted using a single saturating exponential function for given doses <135 Gy and revealed highly uniform behavior. To increase the data set of ages, the natural luminescence signals of the slice fragments used to measure the depth profile were interpolated onto standardized dose-response curves created for each specific sample. Luminescence data from slice fragments showing a signal 3 times greater than the bleaching plateau level were discarded as outliers (the causes of intra-sample heterogeneity are discussed below).

We confirmed the suitability of our measurement approach by carrying out a dose recovery test on samples that yielded suitable bleaching profiles. We bleached rock slices from within the saturated plateau region of each sample (i.e., >1.5 cm depth) for 24 hr in the solar simulator (6 slices/sample) and administered a dose to three of the slices. The dose was then measured using the same protocol as for the D_e measurements described above, with the three un-dosed slices providing an estimation of the residual dose, and the remaining three slices yielding an estimation of the sample's dose recovery. Dose recovery ratios were calculated following subtraction of the residual dose and due to challenging luminescence properties of some samples, the acceptance threshold was set at 25% deviation from unity. A fading test was conducted for each of the samples under investigation, whereby previously measured rock slices were given an 86 Gy dose before preheating and measurement followed by different delay times, following the method of Auclair et al. (2003).
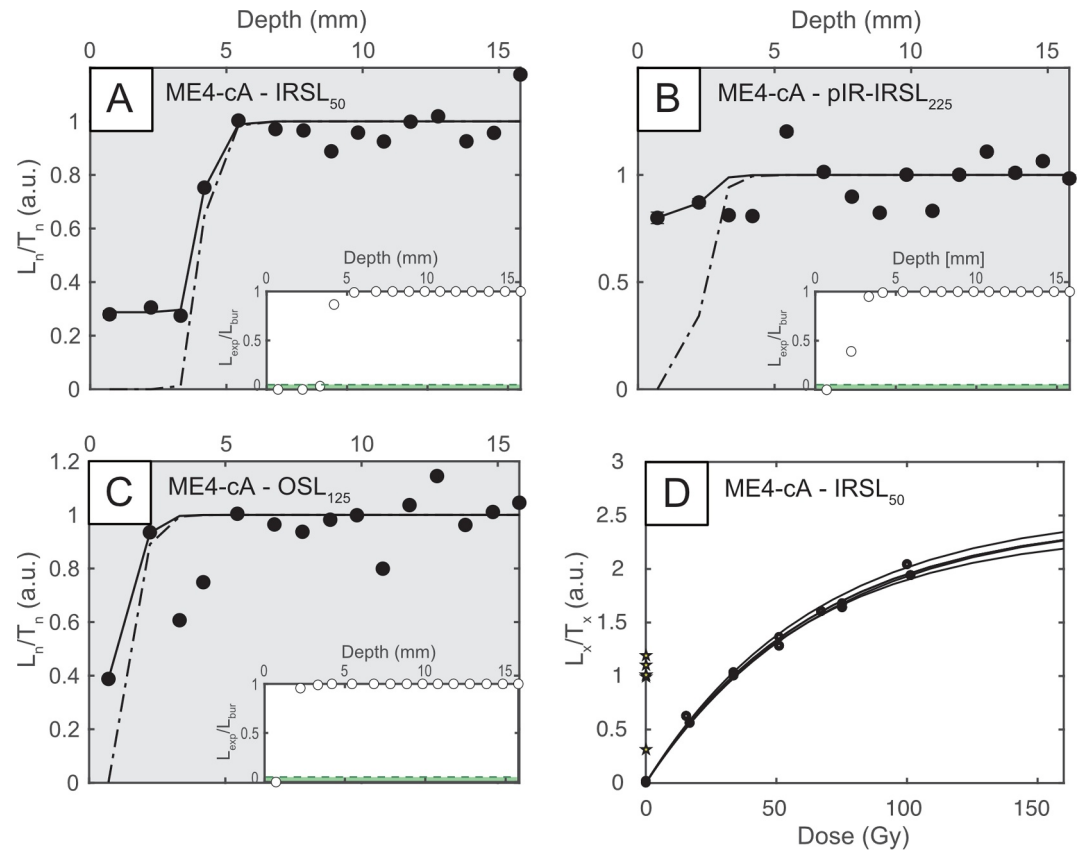
Figure 3. Luminescence data from sample ME4, core A. (a–c) Luminescence depth profiles for the $IRSL_{50}$, $pIR\text{-}IRSL_{225}$ and OSL_{125} signals, respectively. The *x*-axis corresponds to the slice depth and the *y*-axis shows the normalized L_n/T_n ratios of individual slice fragments. The standard errors in the normalized L_n/T_n ratios are within the symbols. The black line and the dashed line correspond to the fit of the natural luminescence signal depth profile (L_{bur}) and the modeled pre-burial luminescence signal exposure (bleaching) profile (L_{exp}), respectively. The inset with the white background shows the ratio L_{exp}/L_{bur} from each slice of the depth profile. The green area below the dashed line corresponds to the acceptance threshold (5%). (d) Dose-response curves used for D_e determination. For each disc fragment, the natural $IRSL_{50}$ signal (black stars) is projected onto the dose-response curve to obtain the D_e.

3.1.3. Environmental Dose Rate Measurements

As the clasts were entrained within ice, zero external dose rate was assumed, with the exception of a cosmic dose contribution calculated for an ice density of 0.9 g cm^{-3} and an assumed depth of 200 m. Whilst for some layers this assumption may not be appropriate as the evolution of the surrounding clast density throughout the transport history of the clast is unknown, we have not accounted for this in our dose rate calculation. We did not account for the potential external dose rate associated with clasts stored in a body of sediment, as this is beyond our current constraints. Such a prolonged storage would imply that our calculated ages are overestimated. We assume a negligible internal water content for the crystalline cobbles of 2 ± 2% based on gneiss free water porosity estimations (Sun et al., 2023). We also assume that the IRSL signals are derived predominantly from K-feldspar minerals within the samples, and that these minerals have a 12.5 ± 0.5% K content (Huntley & Baril, 1997). The size of the K-feldspar minerals was estimated using optical microscopy of each individual sample and ranged from 100–300 μm in sample ME4 to 900–1,000 μm in sample ME8. No internal dose rate was incorporated for OSL ages, which we assume predominantly originate from quartz minerals.

The size range of our cobbles (6–24 cm diameter) means that it is not appropriate to make the infinite matrix assumption for the environmental dose rate, as is commonly done in conventional applications of luminescence dating to sediments. Instead, it is necessary to scale the dose rate to account for the size of the cobble under investigation, the depth of the rock slice within the cobble, and in the case of our samples, to account for the

inactive ice matrix. Following Riedesel and Autzen (2020) and assuming that our cobbles are spherical, the fractional infinite matrix γ-dose rate at the edge of the cobble ($\dot{D}_{edge}$) is given by:

$$\dot{D}_{edge} = 0.5\left(1 - e^{-0.039x}\right) \tag{1}$$

where x is the diameter of the cobble. We calculated the cobble size dependent linear γ-attenuation coefficients following equation S.1 of Riedesel and Autzen (2020) and computed the cobble fractional infinite matrix β- and γ-dose rates using the `calc_CobbleDoseRate()` function (Riedesel & Autzen, 2020) in the R package "Luminescence" (Kreutzer et al., 2012, 2025). These values were then input into DRAC v1.2 (Durcan et al., 2015) to calculate the environmental dose rate using the conversion factors of Guérin et al. (2011) and α-attenuation factors of Brennan et al. (1991); an a-value of 0.08 ± 0.02 was assumed. Full details of the dose rate calculation for individual rock slices are given in the Supporting Information S1.

3.2. Glacier Model Experiments

We used the ice-dynamical glacier landscape evolution model iSOSIA (Egholm et al., 2011) to simulate ice flow, glacier evolution, and sediment transport for the Miage Glacier catchment. iSOSIA is a glacial model that simulates hillslope and glacial erosion, transport, and deposition of sediment, and represents the feedback between supraglacial debris transport, ice flow, and mass balance (Rowan et al., 2015; Scherler & Egholm, 2020). The model version used follows the approach of Scherler and Egholm (2020) and includes a Lagrangian scheme that tracks individual englacial sediment particles through the 3-D model domain. This approach allows the location and properties of each englacial sediment particle (e.g., the source location of the particle, the age of the particle, the duration of time in englacial transport) to be tracked through the simulation. Sediment particles were tracked from production by erosion on hillslopes through glacial transport to deposition in moraines. A set of sensitivity experiments were carried out to determine the most appropriate values to be used to define present-day mass balance, erosion, and sediment transport. Simulations were constrained and evaluated against the current glacier geometry, including the position and relief of medial and ice-marginal moraines (Deline, 1999, 2005), and remote sensing observations of present-day glacier geometry, velocity, and mass balance (Stefaniak et al., 2021). The results of these experiments are presented in the Supporting Information S1.

3.2.1. Model Domain and Mass Balance

The subglacial model domain was defined using the 30-m ASTER GDEM version 2 (2011) from which the estimated present-day ice thickness for all glaciers in the catchment with an area greater than 1 km^2 was subtracted (Farinotti et al., 2019). The model domain was resampled to a grid spacing of 50 m to optimize the model stability and efficiency. Mass balance was described using a temperature-index model to calculate ice ablation and an elevation-dependent distribution of precipitation to calculate snow accumulation. The mass balance defined for the present-day glacier was varied over time in each simulation by changing the mean annual air temperature.

Precipitation was fixed throughout the simulation and the fraction of snowfall relative to rainfall varied with the elevation-dependent air temperature across the model domain such that the rate of accumulation varied with air temperature. To define the initial glacier geometry, a uniform value for precipitation of 1 m a^{-1} was partitioned into snowfall based on the elevation-dependent air temperature for each model time step (Collier et al., 2014). The critical temperature for rain–snow partitioning was set to 0°C (Wijngaard et al., 2019). Accumulation was the result of the total snowfall in each cell and avalanching of snow was imposed for the accumulated snowpack from hillslopes and glacier surfaces steeper than 28° following a steep descent path to redistribute mass across hillslopes and glacier surfaces. Clean-ice ablation (ice melt in mm; M) was calculated with a degree-day factor (DDF) approach (Hock, 2003):

$$\sum_{i=1}^{n} M = DDF \sum_{i=1}^{n} T^{+} \Delta t \tag{2}$$

where air temperature (T) over time (t) was represented by a sine function around a mean annual air temperature at sea level with a seasonal amplitude of 6°C and distributed across the model domain using a lapse rate of

$-0.006°C \, m^{-1}$. The DDF for ice was set to 2.0 mm water equivalent (w.e.) per day per °C and chosen to fit the simulated glacier to the present-day extent. The model time step varied according to the stability of the ice-flow calculation up to a maximum of 0.1 years.

Where rock debris accumulated on the glacier surface, ablation was adjusted depending on the supraglacial debris thickness to account for the insulation of the ice surface resulting from a debris layer, assuming that sub-debris melt did not increase relative to the clean-ice ablation rate (Rowan et al., 2015). The reduction in ablation beneath supraglacial debris was calculated using a reciprocal function that scaled clean-ice ablation rates calculated using the positive degree day scheme (b_{clean}) to give sub-debris melt rates (b_{debris}) as a function of debris thickness (h) (Anderson & Anderson, 2016; Rowan et al., 2021):

$$b_{\text{debris}} = b_{\text{clean}} \times \frac{h_0}{h + h_0} \tag{3}$$

where h_0 is a constant with a value of 0.2 m representing the characteristic debris thickness at which the reduction in ablation due to insulation by supraglacial debris is 50% of the value for an equivalent clean-ice surface. The value for h_0 was chosen from observations made at Miage Glacier (Fyffe et al., 2020) to represent a continuous debris mantle across the width of the ablation area without features that locally enhance ablation such as ice cliffs and supraglacial ponds (Rowan et al., 2021).

3.2.2. Sediment Production and Tracking

Hillslopes steeper than a critical threshold (28°) were eroded at a rate of 0.001 m a^{-1}, in agreement with erosion rates of headwalls determined for other glacial catchments in the Mont Blanc massif (Lehmann et al., 2020; Sarr et al., 2019). Sediment produced by hillslope erosion was transported from the catchment headwalls using a non-linear hillslope flux model that relates sediment flux to slope (Roering et al., 1999):

$$q_s = \frac{K \nabla b}{1 - \left(\frac{|\nabla b|}{S_c}\right)^2} \tag{4}$$

where q_s is hillslope sediment flux, ∇b is the tangent of the hillslope gradient in radians, S_c is the critical slope, and K is the diffusivity constant that represents linear diffusion over time. A positive value for q_s indicates the sediment flux from the cell and increases rapidly as ∇b approaches S_c where q_s is infinite, which is consistent with the concept of threshold hillslopes (Roering et al., 1999).

Sediment motion across the non-glacierized part of the catchment was calculated on the regular model grid and sediment in englacial transport was tracked using a Lagrangian approach. The simulated glacier contained 10^6 particles to track sediment transport, with particles formed where sediment was entrained into ice from the hillslopes and killed where sediment was deposited from the ice into the landscape. Sediment within the model domain was represented as a thickness in each grid cell until the sediment entered englacial transport. When sediment was in contact with ice, a particle was formed to represent this sediment and to track its progress in three dimensions through the glacier.

3.2.3. Experimental Design

The glacier model was used to simulate the evolution of Miage Glacier through the Holocene (∼12 ka to present). Immediately prior to the Holocene during the Younger Dryas cold period (the Egesen stadial), Miage Glacier was more extensive than at present, and as the climate warmed at the start of the Holocene glaciers across the European Alps lost mass (Ivy-Ochs et al., 2009). Therefore, the starting point for the simulation was a stable ice mass somewhat more extensive than the present-day glacier to represent pre-Holocene conditions. The glacier model was spun up for 1,000 years to reach mass balance equilibrium using a mean annual air temperature at sea level of 9.4°C. This pre-Holocene simulation was then forced to the present day using the Temp12k paleotemperature composite of calibrated records of median annual air temperature for the latitude band 30–60°N (Figure 5), which has a time step of 500 years (Kaufman et al., 2020). This data set gives the mean annual air temperature at sea level and was extrapolated to the model domain using the lapse rate noted above. We note that the last data point in the

Temp12k data set represents 0.25 ka, which we refer to as the present day but which is prior to the Little Ice Age maximum around 1800 CE (Deline, 2005) and therefore does not represent the glacier response to more recent climate change (Stefaniak et al., 2021; Thomson et al., 2000).

4. Results

4.1. Luminescence Results

Nine of the 18 samples analyzed showed a L_n/T_n bleaching plateau within the first 2 to 3 discs for the $IRSL_{50}$ signal, suggesting that the luminescence signal has the potential to date burial duration. Among the nine samples showing a bleaching plateau, seven samples passed the dose recovery test within 25% deviation from unity, and among them four samples passed this test for the $IRSL_{50}$ signal within 10% deviation from unity (ME2, ME4, ME13, and ME23). Three samples showed a bleaching plateau within the first 2 to 3 discs for the $pIR\text{-}IRSL_{225}$ signal. From these, two samples passed the dose recovery test for the $pIR\text{-}IRSL_{225}$ signal within 25% deviation from unity. Five samples showed a plateau within the first 2 to 3 discs for the OSL_{125} signal, of which only one sample passed the dose recovery test for the OSL_{125} signal within 10% of unity. In total, 36% of the schist samples ($n = 11$), 60% of the gneiss samples ($n = 5$) and 100% of the felsic rocks ($n = 2$) analyzed passed the plateau test for the $IRSL_{50}$ signal (Table S2 in Supporting Information S1). After 24 hr bleaching in the solar simulator, typical residual doses ranged from 0 to 5.0 Gy for the $IRSL_{50}$ signal, and are as high as 42% of the natural D_e measured. The dose rate to feldspar ranges from 2.1 ± 0.4 to 6.7 ± 1.2 Gy ka^{-1} and to quartz from 2.4 ± 0.2 to 2.8 ± 0.3 Gy ka^{-1} (calculated for the rock surfaces, full dose rate information is given in the Supporting Information S1). Fading rates for the $IRSL_{50}$ and $pIR\text{-}IRSL_{225}$ signals vary depending on the sample and rock slice fragment, and g-values normalized to 2 days range from 0.06% to 2.24% per decade. As fading rates are within error of 1% per decade for all samples for the $IRSL_{50}$ and $pIR\text{-}IRSL_{225}$ signals, no fading correction was applied (see Supporting Information S1).

Residual-corrected $IRSL_{50}$ ages of slice fragments from the L_n/T_n bleaching plateau range from 0.0 ± 1.0 to 19.0 ± 2.5 ka (Table 1). Whereas residual-corrected $IRSL_{50}$ ages of ME2, ME13, ME14 and ME17 show low intra-sample variability, corresponding ages of ME4, ME18 and ME23 yield a much higher degree of variability between different fragments. Minimum ages from the L_n/T_n plateau for each sample range from 0.0 ± 1.0 to 4.7 ± 0.3 ka, whereas mean ages range from 0.6 ± 0.6 to 13.8 ± 5.8 ka (Figure 4). Generally, samples yielding younger ages show lower absolute intra-sample age variability than older samples. Samples collected in the upper part of the ablation zone yield mean ages ranging from 0.6 ± 0.6 to 1.4 ± 0.7 ka and are thus younger than samples collected near the terminus that produced mean ages from 6.4 ± 2.5 to 7.2 ± 4.5 ka (Figure 4). Residual-corrected $pIR\text{-}IRSL_{225}$ ages of slice fragments from the L_n/T_n bleaching plateau of ME18 and ME23 range from 10.0 ± 2.5 to 41.5 ± 2.1 ka (Table 2), whilst residual-corrected OSL_{125} ages of slice fragments from the L_n/T_n bleaching plateau of ME18 range from 35.6 ± 5.4 to 43.7 ± 13.4 ka (Table 3). Residual-corrected $pIR\text{-}IRSL_{225}$ and OSL_{125} ages are thus older than residual-corrected $IRSL_{50}$ ages obtained for the same samples.

4.2. Glacier Model Results

4.2.1. Comparison of the Simulated Glacier with Present-Day Observations

Model reconstructions of glacier dynamics and change contain uncertainties associated with input data and variables such as the description of the subglacial topography and the mass balance and the description of ice flow in a higher-order model. We followed a similar approach to previous studies that reconstruct glacier behavior and compared the glacier model results against data describing mass balance, ice thickness, and ice flow (e.g., Kirkbride et al., 2023; Rowan et al., 2015, 2021). Where these variables can be measured, we tested the model using all the available data sets, for example, by comparing the impact on the simulated ice thickness of both the subglacial topography estimated by Deline (2002) and Farinotti et al. (2019) as model domains. We tested mass balance variables (Figure 5) and evaluated the model results against a range of existing data (Figure 6) describing the present state of Miage Glacier to identify the simulation that most accurately represented this glacier.

The simulated Miage Glacier decreased in area and volume from the spin-up condition between 13 and 12 ka as the glacier transitioned from pre-Holocene to Holocene conditions (Figure 5a). The position of the simulated ice margin varied by up to 100 m after 10 ka as the transition from the Younger Dryas Stadial to the Holocene was completed. The glacier size at 10 ka was similar to that at the end of the simulation. The glacier reached a

Table 1
Sample Locations, Dose Rates, D_e Values and Luminescence Ages Calculated Using $IRSL_{50}$ Signals

Sample[a]	Longitude[b] (dd)	Latitude (dd)	Lithology	Sample diameter (cm)	Distance from headwall[c] (km)	Error (SD) (km)	Total dose rate[d] (Gy.ka⁻¹)	Error (Gy.ka⁻¹)	D_e $IRSL_{50}$ (Gy)	Error (Gy)	$IRSL_{50}$ age (ka)	Error[e] (ka)	$IRSL_{50}$ residual[f] (ka)	Residual-corrected $IRSL_{50}$ age[g] (ka)	Error (ka)	Mean residual-corrected $IRSL_{50}$ age (ka)	Error (SD) (ka)	n[h]
ME2 s1	6.85003	45.79792	Gneiss	11	4.42	0.04	4.6	1.2	4.8	0.3	1.1	0.1	0.7	**0.3**	**0.1**	0.7	0.5	2
ME2 s2							5.3	1.2	9.0	0.2	1.7	0.0	0.7	1.0	0.0			
ME4 s1	6.854167	45.79233	Schist	6	5.48	0.26	2.1	0.4	32.6	5.0	15.2	2.2	0.0	15.2	2.2	13.8	5.8	5
ME4 s2							2.3	0.4	8.8	3.7	3.8	1.6	0.0	**3.8**	**1.6**			
ME4 s3							2.3	0.4	43.9	5.8	19.0	2.5	0.0	19.0	2.5			
ME4 s2							2.3	0.4	38.2	3.5	16.6	1.5	0.0	16.6	1.5			
ME4 s3							2.3	0.4	33.2	3.4	14.4	1.5	0.0	14.4	1.5			
ME13 s1	6.8255	45.81163	Schist	10	2.76	0.30	3.8	0.4	5.4	0.3	1.4	0.1	0.8	0.6	0.1	0.8	0.8	3
ME13 s1							3.8	0.4	3.7	0.3	1.0	0.1	0.8	**0.2**	**0.1**			
ME13 s2							4.5	0.4	11.1	0.2	2.5	0.0	0.8	1.7	0.0			
ME14 s1	6.8255	45.81163	Schist	24	2.76	0.30	6.7	1.2	6.0	0.3	0.9	0.0	0.7	0.2	0.0	0.6	0.6	6
ME14 s2							7.7	1.2	2.9	8.0	0.4	1.0	0.7	**0.0**	**1.0**			
ME14 s3							7.9	1.2	6.9	0.3	0.9	0.0	0.7	0.1	0.0			
ME14 s2							7.7	1.2	15.9	0.4	2.1	0.0	0.7	1.3	0.0			
ME14 s3							7.9	1.2	17.4	0.3	2.2	0.0	0.7	1.5	0.0			
ME14 s4							8.0	1.2	11.4	0.3	1.4	0.0	0.7	0.7	0.0			
ME17 s1	6.834933	45.80702	Gneiss	22	3.25	0.47	3.8	0.4	7.3	0.3	1.9	0.1	0.9	1.0	0.1	1.4	0.7	5
ME17 s1							3.8	0.4	9.6	0.3	2.5	0.1	0.9	1.6	0.1			
ME17 s1							3.8	0.4	8.9	0.3	2.3	0.1	0.9	1.4	0.1			
ME17 s1							3.8	0.4	5.8	1.7	1.5	0.4	0.9	**0.6**	**0.4**			
ME17 s2							4.2	0.4	14.2	0.3	3.4	0.1	0.9	2.5	0.1			
ME18 s1	6.88579	45.78104	Schist	9	8.53	0.05	3.7	0.9	32.5	2.3	8.7	0.5	0.5	8.2	0.5	6.4	2.5	2
ME18 s2							4.3	0.9	22.7	1.4	5.2	0.3	0.5	**4.7**	**0.3**			
ME23 s1	6.88776	45.78888	Gneiss	6	8.11	0.04	2.9	0.2	25.0	1.5	8.7	0.5	0.9	7.8	0.5	7.2	4.5	8
ME23 s1							2.9	0.2	7.1	1.9	2.5	0.7	0.9	**1.5**	**0.7**			
ME23 s1							2.9	0.2	9.8	1.6	3.4	0.6	0.9	2.5	0.6			
ME23 s2							3.3	0.2	34.5	1.9	10.3	0.6	0.9	9.4	0.6			
ME23 s2							3.3	0.2	23.7	1.6	7.1	0.5	0.9	6.1	0.5			

Table 1
Continued

Sample[a]	Longitude[b] (dd)	Latitude (dd)	Lithology	Sample diameter (cm)	Distance from headwall[c] (km)	Error (SD) (km)	Total dose rate[d] (Gy.ka⁻¹)	Error (Gy.ka⁻¹)	D_e IRSL$_{50}$ (Gy)	Error (Gy)	IRSL$_{50}$ age (ka)	Error[e] (ka)	IRSL$_{50}$ residual[f] (ka)	Residual-corrected IRSL$_{50}$ age[g] (ka)	Error (ka)	Mean residual-corrected IRSL$_{50}$ age (ka)	Error (SD) (ka)	n[h]
ME23 s2							3.3	0.2	52.5	1.8	15.7	0.5	0.9	14.8	0.5			
ME23 s1							2.9	0.2	34.6	1.7	12.1	0.5	0.9	11.1	0.5			
ME23 s2							3.3	0.2	16.8	1.7	5.0	0.5	0.9	4.1	0.5			

[a]One core was analyzed to determine the D_e of each sample, the slice from which the aliquot was taken from is specified after the sample's name. [b]Coordinates are given in WGS84 coordinate system. [c]The distance from the headwall is calculated from the flowlines that intersect the sample locations. The error is the standard deviation of the distance from the headwall calculated from the flowlines that intersect the sample locations. [d]Dose rate for each rock slice. [e]The error of the individual fragment ages is calculated as the ratio of the error in the D_e value to the dose rate. [f]Residual measured for each sample. [g]The minimum residual-corrected age of all fragments is indicated in bold for each sample. [h]Number of rock fragments used to calculate the mean residual-corrected age.
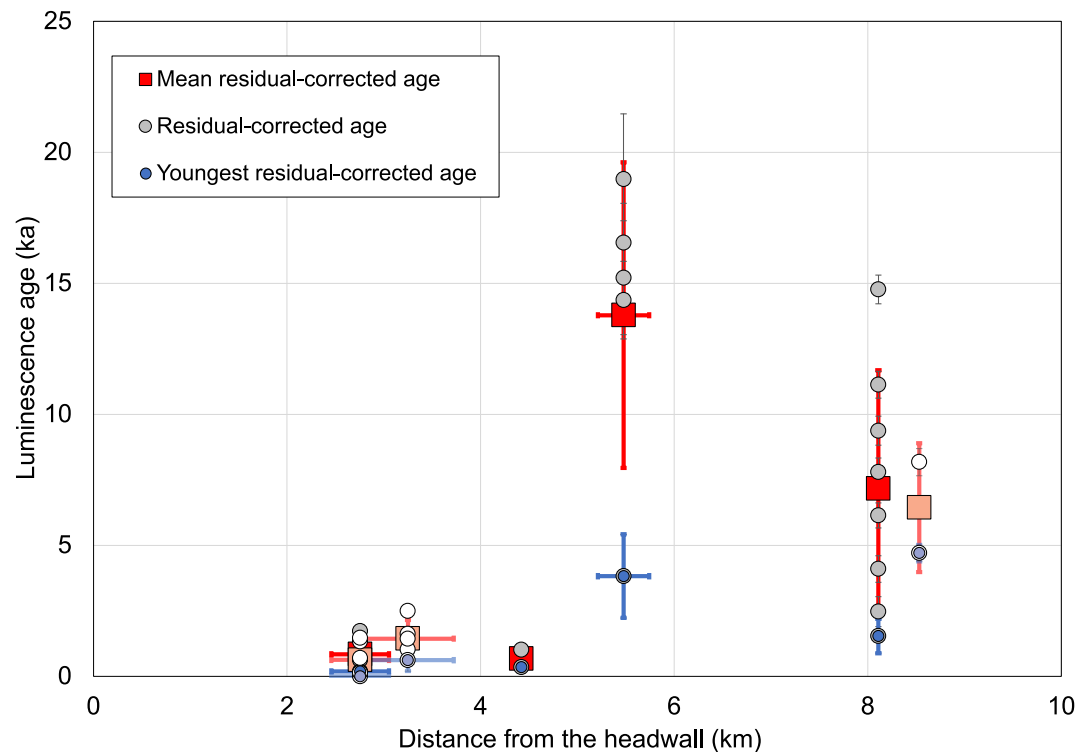
Figure 4. Luminescence burial ages were obtained for englacial rock clasts using the $IRSL_{50}$ signal. Bright colors indicate the four samples that passed the dose recovery test within a 10% deviation from unity, while the three other samples, which passed only within a 25% deviation from unity, are shown in pastel. The distance from the headwall is calculated from modeled flow paths that intersect the sample locations. The standard deviation of the distance from the headwall is calculated from the flowlines that intersect the sample locations.

minimum during the mid-Holocene warm period at 7.2 ka when the maximum ice thickness was 325 m and ice volume was 22% of the present-day value. At the end of the simulation, Miage Glacier had a maximum ice thickness of 339 m, an area of 12.5 km^2 and a volume of 1.2 km^3 (Figure 6a). The corresponding simulated equilibrium line altitude had a median value of 2,603 m and was located close to the base of the convergence of the tributary glaciers with the main valley glacier. The spatial variations of the ELA across the domain (Figure 6c) are explained by snow redistribution through avalanching as other components of the surface mass balance at any given time are functions of elevation.

The simulated ice thickness and surface velocity at the end of the simulation were compared with observations of the present-day glacier. The simulated ice thickness is similar to the estimated distribution described by Farinotti et al. (2019) that was used to create the subglacial model domain (Figure 6a). Slightly greater ice thicknesses between 250 and 350 m were simulated than observed, which reflects that the simulated glacier represents the pre-Little Ice Age glacier, which corresponds to the last temperature of the Temp12k series rather than the glacier in the early 21st Century. Deline (2002) estimated the ice thickness in the ablation area of Miage Glacier, giving some slightly thicker values than the simulated glacier, which also had a greater number of cells where low ice thicknesses occurred due to the difference in extent between the simulated glacier and the extent mapped in the field. Simulated surface velocities had a maximum surface value of 80.9 m a^{-1} in agreement with the observed centerline velocity between 1975 and 1991 (Smiraglia et al., 2000) and a mean of 27.4 ± 12.9 m a^{-1} across the entire glacier in agreement with the mean glacier-wide value between 2017 and 2018 (Stefaniak et al., 2021). The distribution of surface velocities was similar to that observed for Miage Glacier from feature tracking of satellite imagery by Millan et al. (2022), where the simulated and observed surface velocities in the main glacier tongue were about 25 m a^{-1} (Figure 6b). However, the simulated surface velocities in the tributary glaciers are lower than those observed by Millan et al. (2022) because we simulated the tributary glaciers as confluent with the main valley glacier at the end of the Holocene, whereas the observed velocities represent the recent (likely since 1900
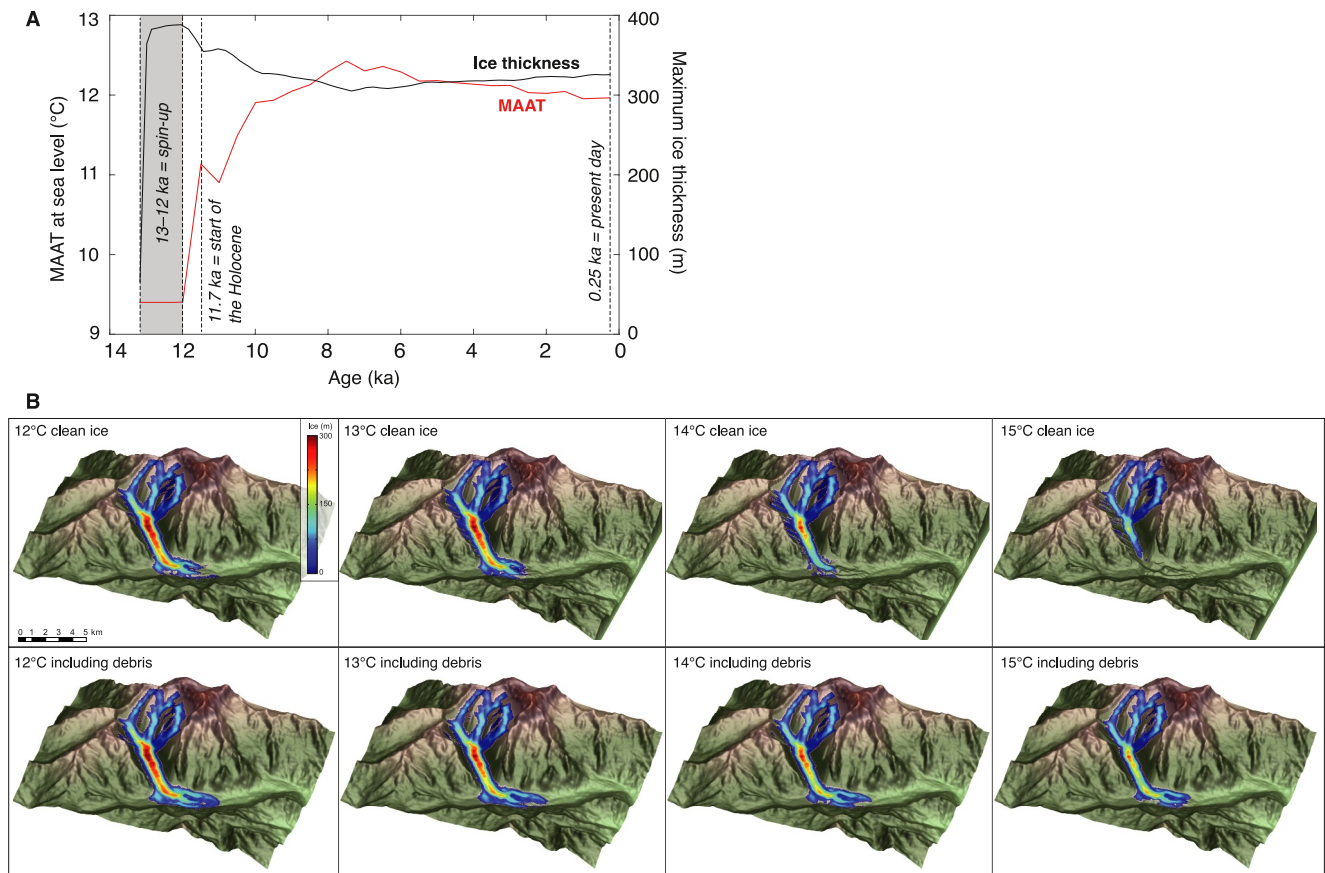
Figure 5. Glacier model experimental design showing (a) the Temp12k Holocene paleotemperature composite used as climate forcing (mean annual air temperature; red line) and the transient glacier response to this climate forcing (maximum ice thickness; black line) simulated from an ice-free domain, and (b) sensitivity test results to determine values for the present-day air temperature at sea level with and without the reduction in ablation resulting from the production and transport of supraglacial debris thickness.

CE) dynamic detachment of the active tributary glaciers from Miage Glacier. The detachment of tributary glaciers reduces the compressional stress toward the terminus and allows the tributaries to overrun the former valley glacier, which is slowing and becoming stagnant in response to recent climate warming. This is evident for Mont Blanc Glacier where the active terminus appears to be disconnected from Miage Glacier (Figure 6b), and likely to also be the case for Bionnassay and Dome Glaciers. Similar dynamic detachment of actively flowing tributary glaciers from debris-covered glacier tongues where ice flow is declining was observed for Khumbu Glacier in the Nepal Himalaya as a precursor to physical detachment of the two sections of the glacier (Miles et al., 2021; Rowan et al., 2021).

The simulated debris mantle had a mean thickness of 0.08 ± 0.24 m (Figure 6d) excluding areas of thick sediment (>2 m) that were in contact with the glacier in the simulation and are associated with the simulated erosion of the steep western headwall located directly above the glacier (Figure 6e). The mean thickness of debris on Miage Glacier from 244 pit measurements made by manual digging in 2006, 2007 and 2018 was 0.14 ± 0.11 m (Rowan et al., 2020). The pit measurements are difficult to compare directly with the simulated debris thickness as the debris cover thickness shows high spatial heterogeneity that the 50-m grid spacing of the glacier model is unable to capture, and there is some bias in the measurement procedure toward areas where debris is more than a few centimeters thick.

4.2.2. Glacial Sediment Transport Flowpaths

The total volume of sediment entrained within the simulated glacier at the present was 4.8×10^6 m^3, which was entirely sourced from hillslope erosion. Most of the simulated sediment (85%) was produced at the start of the

Table 2
Sample Locations, Dose Rates, D_e Values and Luminescence Ages Calculated Using pIR-IRSL$_{225}$ Signals

Sample[a]	Longitude[b] (dd)	Latitude (dd)	Lithology	Sample diameter (cm)	Distance from headwall[c] (km)	Error (SD) (km)	Total dose[d] (Gy.ka^{-1})	Error (Gy.ka^{-1})	D_e pIR-IRSL$_{225}$ (Gy)	Error (Gy)	pIR-IRSL$_{225}$ age (ka)	Error[e] (ka)	pIR-IRSL$_{225}$ residual[f] (ka)	Residual-corrected pIR-IRSL$_{225}$ age[g] (ka)	Error (ka)	Mean residual-corrected pIR-IRSL$_{225}$ age (ka)	Error (SD) (ka)	n[h]
ME18 s1	6.88579	45.78104	Schist	9	8.53	0.05	3.7	0.9	149.8	14.3	40.2	3.8	2.0	38.1	3.8	29.6	12.0	2
ME18 s2							4.3	0.9	100.5	13.4	23.2	3.1	2.0	**21.1**	**3.1**			
ME23 s1	6.88776	45.78888	Gneiss	6	8.11	0.04	2.9	0.2	86.3	8.5	30.1	3.0	1.9	28.2	3.0	26.6	11.5	8
ME23 s1							2.9	0.2	36.2	34.0	12.6	11.9	1.9	10.7	11.9			
ME23 s1							2.9	0.2	34.0	7.3	11.9	2.5	1.9	**10.0**	**2.5**			
ME23 s2							3.3	0.2	128.4	4.9	38.4	1.5	1.9	36.5	1.5			
ME23 s2							3.3	0.2	117.5	5.6	35.1	1.7	1.9	33.2	1.7			
ME23 s2							3.3	0.2	145.0	6.9	43.3	2.1	1.9	41.5	2.1			
ME23 s1							2.9	0.2	92.2	7.4	32.2	2.6	1.9	30.3	2.6			
ME23 s2							3.3	0.2	81.9	7.0	24.5	2.1	1.9	22.6	2.1			

[a]One core was analyzed to determine the D_e of each sample, the slice from which the aliquot was taken from is specified after the sample's name. [b]Coordinates are given in WGS84 coordinate system. [c]The distance from the headwall is calculated from the flowlines that intersect the sample locations. The error is the standard deviation of the distance from the headwall calculated from the flowlines that intersect the sample locations. [d]Dose rate for each rock slice. [e]The error of the individual fragment ages is calculated as the ratio of the error in the D_e value to the dose rate. [f]Residual measured for each sample. [g]The minimum residual-corrected age of all fragments is indicated in bold for each sample. [h]Number of rock fragments used to calculate the mean residual-corrected age.

Table 3
Sample Locations, Dose Rates, D_e Values and Luminescence Ages Calculated Using OSL$_{125}$ Signals

Sample[a]	Longitude[b] (dd)	Latitude (dd)	Lithology	Sample diameter (cm)	Distance from headwall[c] (km)	Error (SD) (km)	Total dose rate (quartz)[d] (Gy.ka^{-1})	Error (Gy.ka^{-1})	D_e OSL$_{125}$ (Gy)	Error (Gy)	OSL$_{125}$ age (ka)	Error[e] (ka)	OSL$_{125}$ residual[f] (ka)	Residual-corrected OSL$_{125}$ age[g] (ka)	Error (ka)	Mean residual-corrected OSL$_{125}$ age (ka)	Error (SD) (ka)	n[h]
ME18 s1	6.88579	45.78104	Schist	9	8.53	0.05	2.3	0.2	113.3	31.5	48.2	13.4	4.5	43.7	13.4	39.6	5.7	2
ME18 s2							3.0	0.3	118.9	16.0	40.1	5.4	4.5	**35.6**	**5.4**			

[a]One core was analyzed to determine the D_e of each sample, the slice from which the aliquot was taken from is specified after the sample's name. [b]Coordinates are given in WGS84 coordinate system. [c]The distance from the headwall is calculated from the flowlines that intersect the sample locations. The error is the standard deviation of the distance from the headwall calculated from the flowlines that intersect the sample locations. [d]Dose rate for each rock slice. [e]The error of the individual fragment ages is calculated as the ratio of the error in the D_e value to the dose rate. [f]Residual measured for each sample. [g]The minimum residual-corrected age of all fragments is indicated in bold for each sample. [h]Number of rock fragments used to calculate the mean residual-corrected age.
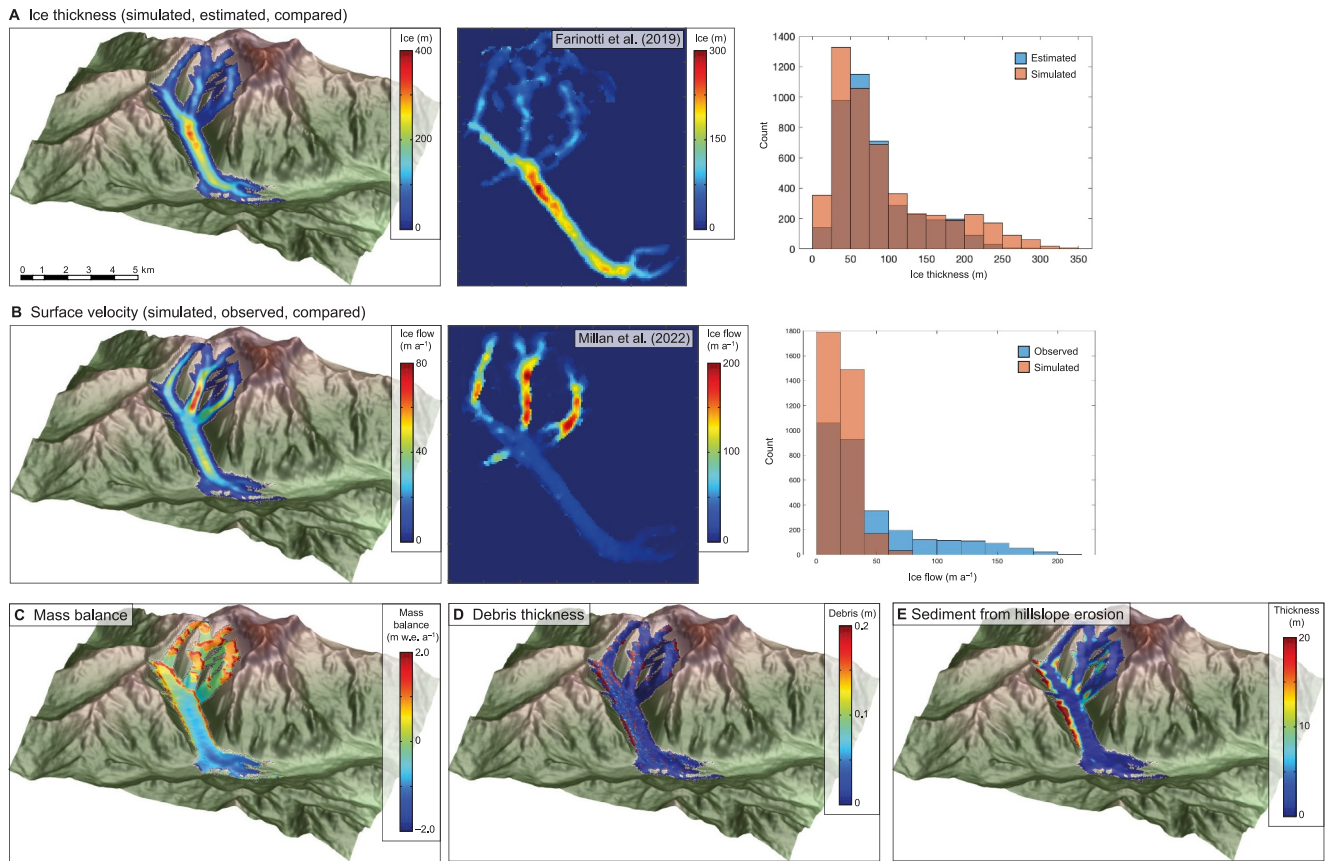
Figure 6. Summary of glacier model results for the end of the Holocene simulation showing (a) simulated ice thickness compared with estimated ice thickness from Farinotti et al. (2019), (b) simulated glacier surface displacement (velocity) compared with observed surface velocity from Millan et al. (2022), (c) simulated mass balance, and (d) simulated supraglacial debris thickness less than 0.2 m in thickness, and (e) simulated sediment distribution produced by hillslope erosion.

simulation as oversteepened hillslopes were eroded following deglaciation after the Younger Dryas Stadial. The remaining sediment (15%) was produced during the Holocene from hillslopes that remained steeper than the critical threshold. Sediment was entrained by the glacier along the ice margins and at the glacier bed. Sediment was then either transported within the ice or on the glacier surface as medial moraines. Sediments that were in contact with the glacier were treated as particles that were tracked through the ice over time. The model always contained 10^6 particles, many of which followed the same route through the glacier. The particle tracking computed 950 3-D sediment flowlines (Figure 7a) that intersected the ice surface and thus could have transported clasts to the sample locations, of which 764 flowlines were at least 1 km in length and represented ice flow within the glacier rather than only within ice aprons or ice patches on the hillslopes. Sediment transport over distances greater than 1 km did occur within the ice-marginal areas, as represented by the fraction of the flowlines (125 flowlines; 16% of the total) contained within small areas of ice near the margins of the terminal lobes for the entire duration of the simulation. These areas gave long transport distances representing only a small horizontal displacement from their final location within the model domain and were taken to represent the reworking of sediment on the proximal slopes of ice-marginal moraines and as such were excluded from further analysis. Of the remaining particles, the pathways and time taken for sediment to be transported through the glacier and the distance traveled were variable and divided into three groups.

1. 24% (186 flowlines) of particles did not leave the accumulation area and remained in storage on the hillslopes around and within the steep sections of the tributary glaciers for hundreds to thousands of years (flowlines from group 1 are indicated in red on Figure 7).

2. 66% (503 flowlines) of particles were transported in the upper 10% of the ice column for at least 1 km, and in most cases for at least 50% of the glacier length (flowlines from group 2 are indicated in blue on Figure 7). Most of these particles moved through the entire glacier length within several hundred years and were then
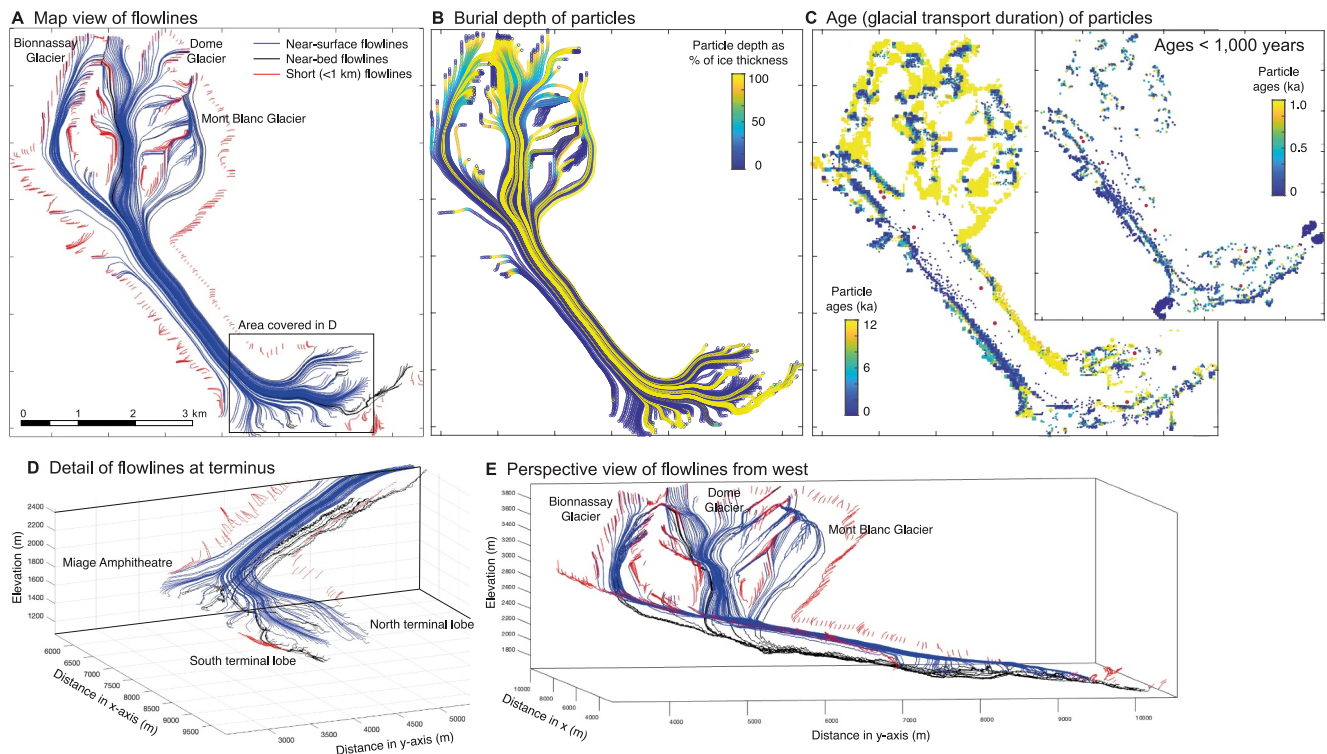
Figure 7. Simulated sediment particle flowlines and transport durations showing (a) flowlines in map view and (b) particles colored by their depth in the ice column in map view. Multiple particles are shown for many points on the model domain and the particles transported lower in the ice column are superimposed upon those transported near the ice surface. (c) The age (glacial transport duration) of particles with the inset showing only those particles with ages less than 1,000 years. (d) Flowlines through the terminus area in detail looking upglacier, and (e) a perspective view of the flowlines from the true right (west) of the glacier. Flowlines through Miage Glacier that intersect the ice surface at their end point are shown for those that are less than 1 km in length (red lines) and 1 km or longer that flow near the glacier surface (blue lines) or close to the glacier bed (black lines).

deposited to form moraines. Where these particles were significantly older than several hundred years, they had been mobilized from storage within cold-based ice in the accumulation area before being transported englacially down the glacier.

3. 10% (74 flowlines) of particles were transported in the lowermost 40% of the ice column through at least 60% of the glacier length to reach the ice surface in the terminal lobes (flowlines from group 3 are indicated in black on Figure 7). The geometry of the termini controlled the emergence paths of these particles, which were all several thousand years in age.

The particles close to the glacier bed traveled a greater total distance relative to their horizontal displacement downglacier than those higher in the ice column because these particles traveled further vertically through the ice column from the uppermost parts of the glacier, whereas particles with shallower flowpaths often entered the glacier closer to the equilibrium line (Figure 7b). The particles transported lower in the ice column also had less direct flowpaths due to the roughness of the glacier bed (Figure 7e). The mean transport duration for near-surface flowlines was about 300 years although some longer flowlines indicated transport durations of approximately 1,000 years. In contrast, the mean transport duration for near-bed flowlines was about 2,000 years, representing an order of magnitude longer duration of glacial sediment transport rather than an extended period of sediment storage within the glacial catchment.

5. Discussion

5.1. Limitations of the Combined Experimental Approach and Potential Future Improvements

The glacier model did not consider the stochastic effect of individual rock avalanches onto the glacier surface, which could be important in determining the timing of sediment delivery to the glacier surface, but rather was treated as a constant value for the entire simulation. We consider that this time-averaging of rock avalanching is

within the uncertainties associated with the temporal resolution of the luminescence rock surface burial ages and the glacier model results. Sediment production in the glacier model did not include erosion of the bed (e.g., by abrasion or quarrying) as we do not consider the clasts measured using luminescence to be subglacially sourced; such clasts would be expected to have no prior history of exposure to sunlight and therefore show a saturated luminescence signal. As we do not include subglacial erosion in the model experiments, we excluded the modification of the glacier bed from the processes that influence the evolution of the glacier and the landscape. The simulated flux of sediment to the glacier is likely to be somewhat smaller than the total catchment denudation during the Holocene as the destabilization of headwalls by glacial undercutting is not considered. Deline (2002) estimated the subglacial erosion rate of Miage Glacier to be around 1.5 mm a^{-1}, which would give 18 m of denudation if this rate were constant throughout the Holocene. However, Deline (2002) also noted from geophysical observations the presence of subglacial sediment about 10–20 m in thickness in the lower ablation area and suggested that, assuming a constant rate, the long-term subglacial erosion rate is half that estimated. The effect of changing the geometry of the glacier bed on glacier evolution is therefore expected to be within the uncertainty associated with the derivation of the subglacial topography.

5.2. Luminescence Rock Surface Burial Dating of Glacial Sediment Transport

Half of the samples analyzed do not show a plateau for the $IRSL_{50}$ signal. A sample's surface that does not exhibit a plateau is indicative of insufficient bleaching of the luminescence signal, suggesting that the sample was not extensively exposed to daylight before its burial. For 10 samples, two surfaces were cored, implying that the five samples without a plateau in the two cores analyzed were not bleached. This suggests that these clasts may originate from larger rocks that are broken down just before burial in the accumulation zone of the glacier or within the ice or that they had a very short residence on the headwalls. The values of the residual doses after 24 hr bleaching in the solar simulator (0–5 Gy) and the short length of the L_n/T_n plateau (2–3 mm) suggest that the samples from the Miage catchment were hard to bleach. More specifically, most schist samples (64%) did not show a plateau for the $IRSL_{50}$ signal, indicating either that schists are the hardest to bleach lithology in the Miage catchment or that they are the most likely to break down before or during englacial transport. Removal of material from the clast surfaces (erosion) would remove the bleaching profile, making a clast appear unbleached (e.g., Lehmann et al., 2020; Sohbati et al., 2018). In addition, the abundance of mafic minerals within the schists and the ~90° coring angle with respect to the schistosity (necessary in some cases to avoid core breakage) could explain the lack of bleaching of these samples (e.g., Ou et al., 2018). Residual doses of the samples investigated were significant, equating to up to ~40% of the D_e value for the $IRSL_{50}$ signal. Consequently, all ages have been residual-subtracted using a sample-specific residual dose measured following bleaching in a solar simulator. Whilst we acknowledge that the true residual dose may differ, the lack of independent data constraining the ages of englacially transported debris, and the novel application of luminescence dating to inform englacial burial ages means that even low precision luminescence ages are of value. However, we recommend that in future studies catchments with (a) more quartz- and feldspar-rich lithologies and (b) lighter color rocks are targeted, where the residual doses may be smaller, and the plateau may extend to greater depths due to the increased ease of bleaching lighter color lithologies (e.g., Ou et al., 2018).

We note that residual-corrected $IRSL_{50}$ ages are younger than pIR-$IRSL_{225}$ and OSL_{125} ages. This inconsistency may be attributed to a higher residual dose pre-burial (e.g., Kars et al., 2014; Zhang et al., 2015). Additionally, the OSL_{125} signal likely reflects a mix of quartz and feldspar rather than a pure quartz signal, and the high-temperature IRSL measurement may have removed the fast component of the quartz signal (e.g., Fan et al., 2009; Jain et al., 2005). For this reason, and in the absence of alternative age control, we consider the residual-corrected $IRSL_{50}$ ages in our data set to be most representative of the burial duration. Despite fulfilling the plateau test (al Khasawneh et al., 2019), residual-corrected ages from the bleaching plateau show high intra-sample variability for 50% of the samples. Furthermore, the scatter in single aliquot residual-corrected ages, determined both for the slice fragments used to calculate the L_n/T_n ratios of the bleaching profile as well as additional fragments of the same slices, is greater than the scatter in the L_n/T_n plateau. This could indicate mineralogic heterogeneity that promotes non-uniform bleaching within the same slice (Meyer et al., 2018). Additionally, given the mineralogic heterogeneity, the dose rate and fading rate likely vary, explaining intra-slice variability of the ages. Dose rates are calculated at the scale of the cobble rather than the individual slice fragment, which is likely to have a significant influence on the age distribution (e.g., Ou et al., 2022; Souza et al., 2019). For samples ME2, ME13 and ME17, the $IRSL_{50}$ signal of the L_n/T_n bleaching plateaus exhibits an increasing trend

with depth; a potential explanation could be that the luminescence signals are partially bleached although they fulfill the requirement that the pre-burial signal is <5% of the burial signal (al Khasawneh et al., 2019). Given that our L_n/T_n bleaching plateaus are generally short, we cannot entirely rule out the possibility that the entire slices were not perfectly bleached due to mineralogical heterogeneity before burial. Therefore, to avoid potential inheritance from partial bleaching, we consider the youngest $IRSL_{50}$ burial ages in our data set to be most representative of the clast transport histories, but all ages are provided for transparency (Figure 4 and Tables 1–3). We suggest that in the case of samples bearing a short L_n/T_n bleaching plateau, the use of the first rock core slice(s) should be favored for age determination. The use of study sites characterized by feldspar-rich lithologies that are easier to bleach would improve the robustness of the luminescence results.

5.3. Modeling Glacier Evolution and Sediment Transport Through the Holocene

Our simulation of Miage Glacier was forced by a regional subset of the Temp12k paleotemperature composite (Figure 5a; Kaufman et al., 2020) and started with deglaciation after the Younger Dryas Stadial when large volumes of sediment were produced in the model by hillslope erosion. This release of sediment reproduced the expected increase in sediment flux resulting from debuttressing of steep hillslopes and the release of sediment produced by glacial erosion during the earlier advance (Lane et al., 2017). Stefaniak et al. (2021) determined geodetic mass balance for Miage Glacier between 1990 and 2018 from satellite observations of surface elevation change, that are reported therein as a glacier-wide mean value of -0.86 ± 0.27 m w.e. a^{-1}. The simulated present-day glacier-wide mass balance was 0.004 ± 0.94 m w.e. a^{-1}. However, these observations are difficult to compare quantitively with the simulated mass balance as the geodetic measurements are strongly influenced by short-term changes in the glacier surface, for example, the evolution of the debris layer and supraglacial ponds, and the glacier model considered a different period in the glacier history prior to the Little Ice Age and more completely represents the redistribution of snow in the accumulation area (Figure 6c).

The glacier model simulations do not include forcing representing the rapid loss of mass from Miage Glacier since the 1990s (Stefaniak et al., 2021; Thomson et al., 2000). We note that the formation of a debris mantle occurs in response to a change to a net negative mass balance forced by sustained increasing air temperatures (Benn et al., 2012; Rowan et al., 2015). This change promotes an enhancement in surface ablation leading to greater exhumation of englacial debris and a reduction in ice flow such that debris cannot be efficiently exported to the ice margins (Kirkbride, 2000). The development of an extensive debris mantle insulates the underlying ice and can reduce ablation sufficiently to cause the glacier tongue to maintain a greater ice volume than a climatically equivalent clean-ice glacier (Figure 5b). As such, moraines formed by debris-covered glaciers may be erroneously attributed to a phase of cooling climate rather than identified as part of a time-transgressive response to a warming climate (Anderson & Anderson, 2016; Rowan et al., 2015). These feedback are implemented in our model but are only weakly observed in terms of their impact on the Holocene evolution of Miage Glacier. The phases of negative mass balance imposed by the climate forcing are less extreme than the current state of this glacier; therefore, supraglacial debris mantles are short-lived and the simulated debris is efficiently transported to ice-marginal moraines over decadal time scales (Figure 6d).

From historical artistic and scientific works, we know that the current debris mantle on Miage Glacier initiated after the Little Ice Age around 1850 CE and expanded to reach the present-day extent in the 1930s (Deline, 2005). The Temp12k data set has a 500-year time interval and ends 250 years before the present day without an excursion representing the Little Ice Age between 1760 and 1830 CE when glaciers in the Alps advanced (Vincent et al., 2005). As a result, our simulation does not reproduce the extensive debris mantle currently observed on the surface of Miage Glacier that is known to have formed after the Little Ice Age (Deline, 2005). Furthermore, the climate forcing does not result in prolonged periods of strongly negative net mass balance that would promote the development of such debris layers earlier in the Holocene. Therefore, despite the large sediment flux to the glacier from hillslopes, the simulated glacier surface was only partly debris mantled (Figure 6d), suggesting that for most of the Holocene, the glacier could efficiently transport sediment and form large ice-marginal moraines.

An order of magnitude more sediment was delivered to the glacier from the western side of the valley in the ablation area from the eastern slopes of the Aiguilles de Tré-la-tête because the erosion law is slope-dependent and at the start of the simulation these slopes were steeper than those on the other side and so underwent a greater duration of erosion (Figure 6e). Sediment was then delivered to the glacier surface from the hillslopes by landsliding and there was also a minor supply of sediment directly to the ablation area from the reworking of the
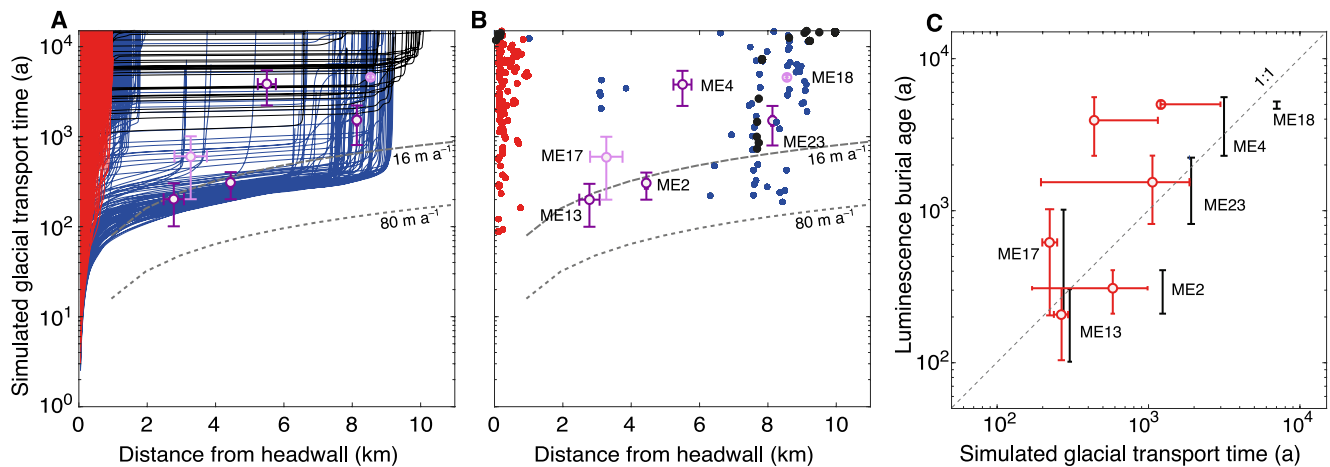
Figure 8. Flowlines that intersect the surface of the Miage Glacier at their end point and associated predicted englacial transport time and luminescence burial ages. (a) Transport time of a particle as it travels along a flow line for each flow line. Red lines are flowlines less than 1 km in length, blue lines are flowlines greater than 1 km in length and above the glacier bed, black lines are subglacial flowlines. (b) Distribution of total time that the particle is transported by ice and distance traveled represented by each englacial flow line. Red dots correspond to flowlines less than 1 km in length, blue dots correspond to flowlines greater than 1 km in length and above the glacier bed, black dots correspond to subglacial flowlines. Luminescence ages are shown as the minimum age for each sample and uncertainty from this value. Bright purple indicates the four samples that passed the dose recovery test within a 10% deviation from unity, while the other samples, which passed only within a 25% deviation from unity, are shown in pastel. The standard deviation of the distance from the headwall is calculated from the flowlines that intersect the sample locations. The gray dashed lines show the clast transport time estimated from the observed glacier surface velocity values. The names of the samples are indicated. (c) Simulated englacial transport duration compared with luminescence burial age for each sample, where the luminescence burial ages are the minimum values and the simulated transport durations are the mean age (red) and the maximum age (black) values. Error bars for the mean simulated transport durations represent one standard deviation of the values for all the flowlines that pass within a 10 m diameter circle centered on the sample location. Note that ME14 has a minimum sample age of 0.0 ± 1.0 ka and so is not shown in this figure.

proximal slopes of ice-marginal moraines. The true-left lateral moraine (on the eastern side of the glacier) and terminal moraines contained a greater number of older particles than the true-right lateral moraine due to the greater flux of young sediment from the western side of the catchment (Figure 7c).

The glacier modeling approach used in this study is similar to that used by Scherler and Egholm (2020) to predict the accumulation of the cosmogenic nuclide Be-10 along the medial moraine of Chhota Shigri Glacier in the Indian Himalaya. In this study, we predict the age of each clast at particular sample locations to independently compare simulated particle transport durations with measured clast rock surface burial ages. We note that the luminescence signal records the duration of clast burial, either within ice or a body of sediment, rather than exposure at the topographic surface, as is the case with Be-10 exposure dating. The simulated particle ages (Figure 7c) indicate significant spatial variability in the age of clasts contained within the ice-marginal moraines of Miage Glacier. As a result, exposure ages for moraines containing supraglacial debris may appear significantly older than expected due to the long duration of glacial sediment transport (Scherler & Egholm, 2020).

5.4. Glaciological Context of the Luminescence Rock Surface Burial Ages

We can compare the integrated transport and storage time represented by each particle in the glacier model with the luminescence rock surface burial ages, as both the simulated particles and the luminescence sample ages predict the duration of time that the clast was transported within or beneath the glacier after it was produced by erosion. The simulated particles that reached the ice surface within a 5-m radius of a luminescence sample location were used to estimate the expected transport history of the sample. The luminescence burial ages generally increased as the samples got closer to the terminus from 0.0 ± 1.0 to 4.7 ± 0.3 ka for the residual-corrected minimum ages and are in agreement with corresponding particle transport durations simulated using the glacier model (Figures 8a and 8b), suggesting that luminescence rock surface burial dating can be used to infer glacial sediment transport duration. Furthermore, the rock surface burial ages produced for each of the luminescence samples generally agree with the particle transport durations simulated using the glacier model, albeit with large associated uncertainties (Figure 8c).
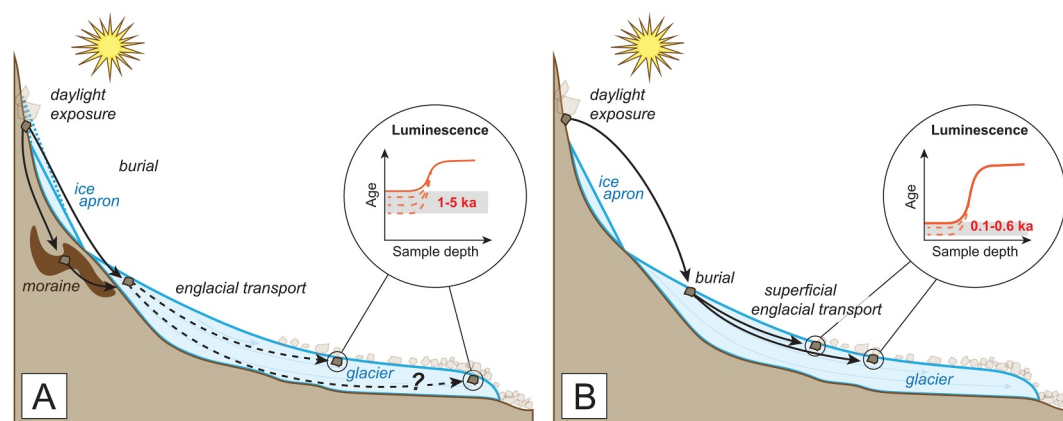
Figure 9. Schematic view of debris transport in a glacial catchment and processes controlling luminescence rock surface burial ages. (a) Older samples are associated with either or both rock debris storage on hillslopes and moraines and transport in the lower part of the ice column where the duration of ice flow is greater than at the glacier surface. (b) Younger samples are characterized by transport in the upper part of the ice column where the particle flowpaths are shorter and the rate of ice flow is faster than at greater depth. The youngest samples were observed in the upper part of the ablation zone and the oldest samples, which were typically an order of magnitude older, were collected from the terminal lobes of Miage Glacier.

The particle flowpaths indicate the routes taken through the glacier to reach the locations where each of the luminescence samples were collected. Four of the luminescence samples (ME2, ME4, ME18 and ME23) were routed from the simulated Dome Glacier flow set that extends from the southern side of Mt Blanc into both terminal lobes of Miage Glacier (Figure 7). The remaining three luminescence samples (ME13, ME14 and ME17) were routed from the Bionnassay Glacier flow set that extends from between the Col de Miage and the Aiguille de Bionnassay to the southernmost margin of Miage Glacier around the Miage Amphitheater moraines where some flowlines terminate (Figure 7), showing a configuration similar to the periods during the Neoglacial when these moraines were formed (Deline and Orombelli, 2005).

The minimum single-aliquot residual-corrected ages of samples in the upper and middle part of the ablation area ranged from 0.0 ± 1.0 to 0.6 ± 0.4 ka (ME2, ME13, ME14 and ME17). We compared the locations of these samples with all the simulated particle flow paths, which indicated that these samples lie within the near-surface ice (Figure 6). The burial ages can then be used to constrain the duration of englacial transport of sediment, which is likely to be similar to the glacier surface displacement unless the sediment has been stored on hillslopes and potentially within areas of cold-based ice, such as ice aprons (Figure 9a). This may be the case for ME17, which was collected close to the confluence with the small, steep Tête Carrée Glacier.

Sample ME4 was collected in the center of the ablation area and gave a minimum single aliquot residual-corrected age of 3.8 ± 1.6 ka. The particle flowlines that intersect the location of this sample all indicate near-surface transport preceded by a long period of storage in the upper part of the catchment within cold-based ice (Figure 7). The results suggest that ME4 was stored in the accumulation area for several thousand years before being entrained in the ice and transported to the ablation area (Figure 9a). Alternatively, the luminescence rock surface burial age for this sample could be explained by the glacier having reworked material that was exposed and buried before being entrained in the ice, such as debris stored on the hillslope at the junction between Bionnassay Glacier and Dome Glacier. However, the glacier model results support the former assumption, as the simulated particles that pass through the sample location had been stored in the upper accumulation area for at least 2,500 years prior to englacial transport to the ablation area (Figure 8a).

Samples ME18 and ME23 were collected from each of the two main terminal lobes of Miage Glacier and gave residual-corrected minimum ages of 4.7 ± 0.3 ka (ME18) and 1.5 ± 0.7 ka (ME23). Both samples are located within the simulated Dome Glacier flow set, as the sharp bend to the east of the glacier tongue in the lower ablation area into the Aosta Valley forces the simulated Bionnassay Glacier flow set on the western side of the glacier to pinch out and the subglacial flowlines on this side of the glacier to emerge close to the Miage

Amphitheater moraines (Figures 7d and 7e). The Dome Glacier flow set and the more minor Mont Blanc Glacier flow set contribute most of the ice flux to the main terminal lobes. The eastward bend of the terminus coupled with the reduction in ice thickness toward the glacier's terminus generates extensional flow and upwelling ice. This dynamic forces the simulated englacial sediment particles to emerge at the glacier's surface in this region. The particle flowlines indicate that samples ME18 and ME23 are the only clasts that could have been transported either through the near-surface ice after a period of storage on the hillslopes or at depth close to the glacier bed as both sets of flowlines terminate at the sample locations (Figures 7e and 9b).

The luminescence rock surface burial ages are considerably older than those reported from the tracking of the bodies of mountaineers or radionuclide contamination that consider the transport of particles deposited on glacier surfaces in the 1920s and 1950s (Jouvet et al., 2020; Jouvet & Funk, 2014). We can roughly estimate the englacial transport duration of sediment close to the glacier surface by integrating the velocities obtained from feature-tracking of glacier surface displacement across the entire glacier length and assuming that these are representative over the duration of particle transport (although this is unlikely to be the case). Using the maximum surface displacement value of 80 m a^{-1} between 1975 and 1991 (Smiraglia et al., 2000) gives a transport duration for a clast sourced from the headwall of the Dome Glacier at the glacier terminus of 131 years, while using the mean annual surface velocity of 16 m a^{-1} between 2017 and 2018 (Stefaniak et al., 2021) gives a transport duration at the glacier terminus of 656 years, assuming that the mean surface velocity value is constant along the entire glacier length, that is in agreement with three of the luminescence ages all of which were transported close to the ice surface (Figures 8a and 8b). These values approximate the limits of the duration of sediment transport near or at the surface of the present-day glacier, but do not represent the history of sediment transport through the Holocene, when ice flow velocities differed from present-day values, or the duration of sediment transport deeper in the ice column where flowpaths are much longer and the ice flow velocities are lower (Mölg et al., 2019; Wijngaard et al., 2019; Zekollari et al., 2014). However, present-day surface velocities for Miage Glacier reflect that the glacier has undergone sustained mass loss and terminus stagnation since the 1990s (Stefaniak et al., 2021) as ice flow during the Little Ice Age would likely have been more rapid than at present and prior to the Little Ice Age during the Medieval Warm Period.

6. Conclusions

We applied a novel approach using luminescence rock surface burial dating to constrain the duration of glacial transport of rock clasts through Miage Glacier, Italy. The burial duration inferred from luminescence measurements on seven clasts was taken to represent the duration of transport of each clast within glacier ice. We compared the clast burial ages measured using luminescence with glacial sediment particle transport times simulated using a Lagrangian scheme implemented in an ice-flow model. In the context of englacial sediment transport, rock clasts should behave in the same way as sediments of different grain sizes. Consequently, our results demonstrate that the duration of sediment transport through Miage Glacier varies across an order of magnitude between sediment transported rapidly in the near-surface ice compared to sediment transported in the lower part of the ice column where flowpaths are longer and the duration of transport is greater due to basal velocities that are lower than velocities higher in the ice column and roughness at the ice-bed interface. The total duration of sediment transport from the headwalls to the glacier ablation area in some cases includes storage phases, as the sediments were either stored within cold-based ice in the accumulation area or ice-marginal moraines in the ablation area for several thousand years before transport in the upper part of the ice column. These results illustrate the different routes by which glaciers transport sediment and provide the first measurements of the duration of sediment transport within an alpine glacier. This study constitutes a proof of concept, highlighting the potential of luminescence rock surface burial dating to determine englacial sediment transport times.

Data Availability Statement

Animations of glacier model results are available from Zenodo (Rowan, 2024a).

The source code for the iSOSIA model (spm-3.4.8) and a test simulation for Miage Glacier are available from Zenodo (Rowan, 2024b).

The luminescence data and MATLAB codes used for data analysis are available from Zenodo (Margirier et al., 2025).

References

al Khasawneh, S., Murray, A., & Abudanah, F. (2019). A first radiometric chronology for the Khatt Shebib megalithic structure in Jordan using the luminescence dating of rock surfaces. *Quaternary Geochronology*, *49*, 205–210. https://doi.org/10.1016/j.quageo.2018.02.007

Anderson, L. S., & Anderson, R. S. (2016). Modeling debris-covered glaciers: Response to steady debris deposition. *The Cryosphere*, *10*(3), 1105–1124. https://doi.org/10.5194/tc-10-1105-2016

Anderson, R. S. (2000). A model of ablation-dominated medial moraines and the generation of debris-mantled glacier snouts. *Journal of Glaciology*, *46*(154), 459–469. https://doi.org/10.3189/172756500781833025

Anderson, R. S., Anderson, L. S., Armstrong, W. H., Rossi, M. W., & Crump, S. E. (2018). Glaciation of alpine valleys: The glacier – debris-covered glacier – rock glacier continuum. *Geomorphology*, *311*, 127–142. https://doi.org/10.1016/j.geomorph.2018.03.015

Auclair, M., Lamothe, M., & Huot, S. (2003). Measurement of anomalous fading for feldspar IRSL using SAR. *Radiation Measurements*, *37*(4–5), 487–492. https://doi.org/10.1016/s1350-4487(03)00018-0

Benn, D. I., Bolch, T., Hands, K., Gulley, J., Luckman, A., Nicholson, L. I., et al. (2012). Response of debris-covered glaciers in the Mount Everest region to recent warming, and implications for outburst flood hazards. *Earth-Science Reviews*, *114*(1–2), 156–174. https://doi.org/10.1016/j.earscirev.2012.03.008

Benn, D. I., & Lehmkuhl, F. (2000). Mass balance and equilibrium-line altitudes of glaciers in high-mountain environments. *Quaternary International*, *65–66*, 15–29. https://doi.org/10.1016/S1040-6182(99)00034-8

Bonani, G., Ivy, S. D., Hajdas, I., Niklaus, T. R., & Suter, M. (1994). AMS ^{14}C age determinations of tissue, bone and grass samples from the Ötztal ice man. *Radiocarbon*, *36*(2), 247–250. https://doi.org/10.1017/S0033822200040534

Brennan, B. J., Lyons, R. G., & Phillips, S. W. (1991). Attenuation of alpha particle track dose for spherical grains. *International Journal of Radiation Applications and Instrumentation*. Part D. *Nuclear Tracks and Radiation Measurements*, *18*(1–2), 249–253. https://doi.org/10.1016/1359-0189(91)90119-3

Buri, P., Miles, E. S., Steiner, J. F., Ragettli, S., & Pellicciotti, F. (2021). Supraglacial ice cliffs can substantially increase the mass loss of debris-covered glaciers. *Geophysical Research Letters*, *48*(6), e2020GL092150. https://doi.org/10.1029/2020GL092150

Chapot, M. S., Sohbati, R., Murray, A. S., Pederson, J. L., & Rittenour, T. M. (2012). Constraining the age of rock art by dating a rockfall event using sediment and rock-surface luminescence dating techniques. *Quaternary Geochronology*, *13*, 18–25. https://doi.org/10.1016/j.quageo.2012.08.005

Collier, E., Nicholson, L. I., Brock, B. W., Maussion, F., Essery, R., & Bush, A. B. G. (2014). Representing moisture fluxes and phase changes in glacier debris cover using a reservoir approach. *The Cryosphere*, *8*(4), 1429–1444. https://doi.org/10.5194/tc-8-1429-2014

Compagno, L., Jouvet, G., Bauder, A., Funk, M., Church, G., Leinss, S., & Lüthi, M. P. (2019). Modeling the Re-appearance of a crashed airplane on Gauligletscher, Switzerland. *Frontiers in Earth Science*, *7*, 170. https://doi.org/10.3389/feart.2019.00170

Dehecq, A., Gourmelen, N., Gardner, A. S., Brun, F., Goldberg, D., Nienow, P. W., et al. (2019). Twenty-first century glacier slowdown driven by mass loss in High Mountain Asia. *Nature Geoscience*, *12*(1), 22–27. https://doi.org/10.1038/s41561-018-0271-9

Delaney, I., & Adhikari, S. (2020). Increased subglacial sediment discharge in a warming climate: Consideration of ice dynamics, glacial erosion, and fluvial sediment transport. *Geophysical Research Letters*, *47*(7), e2019GL085672. https://doi.org/10.1029/2019GL085672

Deline, P. (1999). La mise en place de l'amphithéâtre morainique du Miage (Val Vény, Val d'Aoste)/The setting up of the Miage morainic amphitheatre (Val Vény, Valley of Aosta). *Géomorphologie: Relief, Processus, Environnement*, *5*(1), 59–72. https://doi.org/10.3406/morfo.1999.975

Deline, P. (2002). Etude géomorphologique des interactions entre écroulements rocheux et glaciers dans la haute montagne alpine: Le versant sud-est du Massif du Mont Blanc (Vallée d'Aoste, Italie). *PhD thesis, Université de Savoie*.

Deline, P. (2005). Change in surface debris cover on Mont Blanc massif glaciers after the "Little Ice Age" termination. *The Holocene*, *15*(2), 302–309. https://doi.org/10.1191/0959683605hl809rr

Deline, P. (2009). Interactions between rock avalanches and glaciers in the Mont Blanc massif during the late Holocene. *Quaternary Science Reviews*, *28*(11–12), 1070–1083. https://doi.org/10.1016/j.quascirev.2008.09.025

Deline, P., & Orombelli, G. (2005). Glacier fluctuations in the western Alps during the Neoglacial, as indicated by the Miage morainic amphitheatre (Mont Blanc massif, Italy). *Boreas*, *34*(4), 456–467. https://doi.org/10.1111/j.1502-3885.2005.tb01444.x

Durcan, J. A., King, G. E., & Duller, G. A. T. (2015). DRAC: Dose rate and age calculator for trapped charge dating. *Quaternary Geochronology*, *28*, 54–61. https://doi.org/10.1016/j.quageo.2015.03.012

Egholm, D. L., Knudsen, M. F., Clark, C. D., & Lesemann, J. E. (2011). Modeling the flow of glaciers in steep terrains: The integrated second-order shallow ice approximation (iSOSIA): Modeling glaciers where topography is steep. *Journal of Geophysical Research*, *116*(F2), F02012. https://doi.org/10.1029/2010JF001900

Elkadi, J., King, G. E., Lehmann, B., & Herman, F. (2021). Reducing variability in OSL rock surface dating profiles. *Quaternary Geochronology*, *64*, 101169. https://doi.org/10.1016/j.quageo.2021.101169

Fan, A., Li, S. H., & Li, B. (2009). Characteristics of quartz infrared stimulated luminescence (IRSL) at elevated temperatures. *Radiation Measurements*, *44*(5–6), 434–438. https://doi.org/10.1016/j.radmeas.2009.02.019

Farinotti, D., Huss, M., Fürst, J. J., Landmann, J., Machguth, H., Maussion, F., & Pandit, A. (2019). A consensus estimate for the ice thickness distribution of all glaciers on Earth. *Nature Geoscience*, *12*(3), 168–173. https://doi.org/10.1038/s41561-019-0300-3

Foster, L. A., Brock, B. W., Cutler, M. E. J., & Diotri, F. (2012). A physically based method for estimating supraglacial debris thickness from thermal band remote-sensing data. *Journal of Glaciology*, *58*(210), 677–691. https://doi.org/10.3189/2012JoG11J194

Freiesleben, T., Sohbati, R., Murray, A., Jain, M., Al Khasawneh, S., Hvidt, S., & Jakobsen, B. (2015). Mathematical model quantifies multiple daylight exposure and burial events for rock surfaces using luminescence dating. *Radiation Measurements*, *81*, 16–22. https://doi.org/10.1016/j.radmeas.2015.02.004

Fuchs, M., & Owen, L. A. (2008). Luminescence dating of glacial and associated sediments: Review, recommendations and future directions. *Boreas*, *37*(4), 636–659. https://doi.org/10.1111/j.1502-3885.2008.00052.x

Fushimi, H. (1977). Structural studies of glaciers in the Khumbu region. *Journal of the Japanese Society of Snow and Ice*, *39*(Special), 30–39. https://doi.org/10.5331/seppyo.39.Special_30

Fyffe, C. L., Woodget, A. S., Kirkbride, M. P., Deline, P., Westoby, M. J., & Brock, B. W. (2020). Processes at the margins of supraglacial debris cover: Quantifying dirty ice ablation and debris redistribution. *Earth Surface Processes and Landforms*, *45*(10), 2272–2290. https://doi.org/10.1002/esp.4879

Glen, J. W. (1955). The creep of polycrystalline ice. *Proceedings of the Royal Society of London. Series A. Mathematical and Physical Sciences*, *228*, 519–538. https://doi.org/10.1098/rspa.1955.0066

Guérin, G., Mercier, N., & Adamiec, G. (2011). Dose-rate conversion factors: Update. *Ancient Tl*, *29*(1), 5–8. https://doi.org/10.26034/la.atl.2011.443

Hales, T. C., & Roering, J. J. (2009). A frost "buzzsaw" mechanism for erosion of the eastern Southern Alps, New Zealand. *Geomorphology*, *107*(3–4), 241–253. https://doi.org/10.1016/j.geomorph.2008.12.012

Hambrey, M. J., Bennett, M. R., Dowdeswell, J. A., Glasser, N. F., & Huddart, D. (1999). Debris entrainment and transfer in polythermal valley glaciers. *Journal of Glaciology*, *45*(149), 69–86. https://doi.org/10.3189/S0022143000003051

Herreid, S., & Pellicciotti, F. (2020). The state of rock debris covering Earth's glaciers. *Nature Geoscience*, *13*(9), 621–627. https://doi.org/10.1038/s41561-020-0615-0

Hock, R. (2003). Temperature index melt modelling in mountain areas. *Journal of Hydrology*, *282*(1–4), 104–115. https://doi.org/10.1016/S0022-1694(03)00257-9

Hubbard, B., & Sharp, M. (1995). Basal ice facies and their formation in the western Alps. *Arctic and Alpine Research*, *27*(4), 301. https://doi.org/10.2307/1552023

Huntley, D. J., & Baril, M. R. (1997). The K content of the K-feldspars being measured in optical dating or in thermoluminescence dating. *Ancient TL*, *15*(1), 1–13. https://doi.org/10.26034/la.atl.1997.271

Iverson, N. (1993). Regelation of ice through debris at glacier beds: Implications for sediment transport. *Geology*, *21*(6), 559–562. https://doi.org/10.1130/0091-7613(1993)021<0559:roitda>2.3.co;2

Ivy-Ochs, S., Kerschner, H., Maisch, M., Christl, M., Kubik, P. W., & Schlüchter, C. (2009). Latest pleistocene and Holocene glacier variations in the European Alps. *Quaternary Science Reviews*, *28*(21–22), 2137–2149. https://doi.org/10.1016/j.quascirev.2009.03.009

Jain, M., Murray, A. S., Bøtter-Jensen, L., & Wintle, A. G. (2005). A single-aliquot regenerative-dose method based on IR (1.49 eV) bleaching of the fast OSL component in quartz. *Radiation Measurements*, *39*(3), 309–318.

Jenkins, G. T. H., Duller, G. A. T., Roberts, H. M., Chiverrell, R. C., & Glasser, N. F. (2018). A new approach for luminescence dating glaciofluvial deposits - high precision optical dating of cobbles. *Quaternary Science Reviews*, *192*, 263–273. https://doi.org/10.1016/j.quascirev.2018.05.036

Jennings, S. J. A., & Hambrey, M. J. (2021). Structures and deformation in glaciers and ice sheets. *Reviews of Geophysics*, *59*(3), e2021RG000743. https://doi.org/10.1029/2021RG000743

Jouvet, G., & Funk, M. (2014). Modelling the trajectory of the corpses of mountaineers who disappeared in 1926 on Aletschgletscher, Switzerland. *Journal of Glaciology*, *60*(220), 255–261. https://doi.org/10.3189/2014JoG13J156

Jouvet, G., Röllin, S., Sahli, H., Corcho, J., Gnägi, L., Compagno, L., et al. (2020). Mapping the age of ice of Gauligletscher combining surface radionuclide contamination and ice flow modeling. *The Cryosphere*, *14*(11), 4233–4251. https://doi.org/10.5194/tc-14-4233-2020

Kars, R. H., Reimann, T., Ankjærgaard, C., & Wallinga, J. (2014). Bleaching of the post-IR IRSL signal: New insights for feldspar luminescence dating. *Boreas*, *43*(4), 780–791. https://doi.org/10.1111/bor.12082

Kaufman, D., McKay, N., Routson, C., Erb, M., Davis, B., Heiri, O., et al. (2020). A global database of Holocene paleotemperature records. *Scientific Data*, *7*(1), 115. https://doi.org/10.1038/s41597-020-0445-3

Kirkbride, M. P. (2000). Ice-marginal geomorphology and Holocene expansion of debris-covered Tasman glacier, New Zealand. In M. Nakawo, C. F. Raymond, & A. Fountain (Eds.), *Debris-covered glaciers* (Vol. 264, pp. 211–217). IAHS Publication.

Kirkbride, M. P., & Deline, P. (2013). The formation of supraglacial debris covers by primary dispersal from transverse englacial debris bands: Supraglacial cover formation from englacial debris bands. *Earth Surface Processes and Landforms*, *38*(15), 1779–1792. https://doi.org/10.1002/esp.3416

Kirkbride, M. P., Sherriff, S. C., Rowan, A. V., Egholm, D. L., Quincey, D. J., Miles, E., et al. (2023). Provenance and transport of supraglacial debris revealed by variations in debris geochemistry on Khumbu Glacier, Nepal Himalaya. *Earth Surface Processes and Landforms*, *48*(14), 2737–2753. https://doi.org/10.1002/esp.5657

Kreutzer, S., Dietze, M., & Burow, C. (2025). use_DRAC(): Use DRAC to calculate dose rate data. Function version 0.15. R package version 1.0.0. In S. Kreutzer, C. Burow, M. Dietze, M. C. Fuchs, C. Schmidt, M. Fischer, et al. (Eds.), *Luminescence: Comprehensive luminescence dating data analysis*. Retrieved from https://r-lum.github.io/Luminescence/

Kreutzer, S., Schmidt, C., Fuchs, M. C., Dietze, M., Fischer, M., & Fuchs, M. (2012). Introducing an R package for luminescence dating analysis. *Ancient TL*, *30*(1), 1–8. https://doi.org/10.26034/la.atl.2012.457

Lane, S. N., Bakker, M., Gabbud, C., Micheletti, N., & Saugy, J.-N. (2017). Sediment export, transient landscape response and catchment-scale connectivity following rapid climate warming and Alpine glacier recession. *Geomorphology*, *277*, 210–227. https://doi.org/10.1016/j.geomorph.2016.02.015

Lehmann, B., Herman, F., Valla, P. G., King, G. E., Biswas, R. H., Ivy-Ochs, S., et al. (2020). Postglacial erosion of bedrock surfaces and deglaciation timing: New insights from the Mont Blanc massif (western Alps). *Geology*, *48*(2), 139–144. https://doi.org/10.1130/G46585.1

Lejeune, Y., Bertrand, J.-M., Wagnon, P., & Morin, S. (2013). A physically based model of the year-round surface energy and mass balance of debris-covered glaciers. *Journal of Glaciology*, *59*(214), 327–344. https://doi.org/10.3189/2013JoG12J149

Mackintosh, A. N., Anderson, B. M., & Pierrehumbert, R. T. (2017). Reconstructing climate from glaciers. *Annual Review of Earth and Planetary Sciences*, *45*(1), 649–680. https://doi.org/10.1146/annurev-earth-063016-020643

Margirier, A., Brondex, J., Schmidt, C., Rowan, A., & King, G. E. (2025). Codes for luminescence rock surface burial dating and luminescence data of englacial rocks from Miage Glacier [Dataset]. *Zenodo*. https://doi.org/10.5281/zenodo.14720002

Meyer, M. C., Gliganic, L. A., Jain, M., Sohbati, R., & Schmidmair, D. (2018). Lithological controls on light penetration into rock surfaces–Implications for OSL and IRSL surface exposure dating. *Radiation Measurements*, *120*, 298–304. https://doi.org/10.1016/j.radmeas.2018.03.004

Miles, K. E., Hubbard, B., Miles, E. S., Quincey, D. J., & Rowan, A. V. (2022). Internal structure of a Himalayan debris-covered glacier revealed by borehole optical televiewing. *Journal of Glaciology*, *69*(276), 1–12. https://doi.org/10.1017/jog.2022.100

Miles, K. E., Hubbard, B., Miles, E. S., Quincey, D. J., Rowan, A. V., Kirkbride, M., & Hornsey, J. (2021). Continuous borehole optical televiewing reveals variable englacial debris concentrations at Khumbu Glacier, Nepal. *Communications Earth & Environment*, *2*(1), 12. https://doi.org/10.1038/s43247-020-00070-x

Millan, R., Mouginot, J., Rabatel, A., & Morlighem, M. (2022). Ice velocity and thickness of the world's glaciers. *Nature Geoscience*, *15*(2), 124–129. https://doi.org/10.1038/s41561-021-00885-z

Mölg, N., Bolch, T., Walter, A., & Vieli, A. (2019). Unravelling the evolution of Zmuttgletscher and its debris cover since the end of the little ice age. *The Cryosphere*, *13*(7), 1889–1909. https://doi.org/10.5194/tc-13-1889-2019

Nicholson, L., & Benn, D. I. (2006). Calculating ice melt beneath a debris layer using meteorological data. *Journal of Glaciology*, *52*(178), 463–470. https://doi.org/10.3189/172756506781828584

Ou, X. J., Roberts, H. M., & Duller, G. A. T. (2022). Rapid assessment of beta dose variation inside cobbles, and implications for rock luminescence dating. *Quaternary Geochronology*, *72*, 101349. https://doi.org/10.1016/j.quageo.2022.101349

Ou, X. J., Roberts, H. M., Duller, G. A. T., Gunn, M. D., & Perkins, W. T. (2018). Attenuation of light in different rock types and implications for rock surface luminescence dating. *Radiation Measurements*, *120*, 305–311. https://doi.org/10.1016/j.radmeas.2018.06.027

Pedersen, V. K., & Egholm, D. L. (2013). Glaciations in response to climate variations preconditioned by evolving topography. *Nature*, *493*(7431), 206–210. https://doi.org/10.1038/nature11786

Pellicciotti, F., Stephan, C., Miles, E., Herreid, S., Immerzeel, W. W., & Bolch, T. (2015). Mass-balance changes of the debris-covered glaciers in the Langtang Himal, Nepal, from 1974 to 1999. *Journal of Glaciology*, *61*(226), 373–386. https://doi.org/10.3189/2015JoG13J237

Prescott, J. R., & Robertson, G. B. (1997). Sediment dating by luminescence: A review. *Radiation Measurements*, *27*(5–6), 893–922. https://doi.org/10.1016/s1350-4487(97)00204-7

Preunkert, S., McConnell, J. R., Hoffmann, H., Legrand, M., Wilson, A. I., Eckhardt, S., et al. (2019). Lead and Antimony in Basal Ice From Col du Dome (French Alps) Dated With Radiocarbon: A Record of Pollution During Antiquity. *Geophysical Research Letters*, *46*(9), 4953–4961. https://doi.org/10.1029/2019GL082641

Quincey, D. J., Luckman, A., & Benn, D. (2009). Quantification of Everest region glacier velocities between 1992 and 2002, using satellite radar interferometry and feature tracking. *Journal of Glaciology*, *55*(192), 596–606. https://doi.org/10.3189/002214309789470987

Rades, E. F., Sohbati, R., Lüthgens, C., Jain, M., & Murray, A. S. (2018). First luminescence-depth profiles from boulders from moraine deposits: Insights into glaciation chronology and transport dynamics in Malta valley, Austria. *Radiation Measurements*, *120*, 281–289. https://doi.org/10.1016/j.radmeas.2018.08.011

Ravanel, L., Guillet, G., Kaushik, S., Preunkert, S., Malet, E., Magnin, F., et al. (2023). Ice aprons on steep high-alpine slopes: Insights from the Mont-Blanc massif, western Alps. *Journal of Glaciology*, *69*(277), 1275–1291. https://doi.org/10.1017/jog.2023.15

RGI Consortium. (2017). *Randolph Glacier inventory - a dataset of global glacier outlines, version 6. Central Europe*. NSIDC: National Snow and Ice Data Center. https://doi.org/10.7265/4m1f-gd79

Riedesel, S., & Autzen, M. (2020). Beta and gamma dose rate attenuation in rocks and sediment. *Radiation Measurements*, *133*, 106295. https://doi.org/10.1016/j.radmeas.2020.106295

Roering, J. J., Kirchner, J. W., & Dietrich, W. E. (1999). Evidence for nonlinear, diffusive sediment transport on hillslopes and implications for landscape morphology. *Water Resources Research*, *35*(3), 853–870. https://doi.org/10.1029/1998WR900090

Rowan, A., Stewart, R., & Foster, L. (2020). Supraglacial debris thickness measurements from Miage Glacier, Italy [Dataset]. *Zenodo*. https://doi.org/10.5281/zenodo.3971785

Rowan, A. V. (2024a). Animations of glacier model results from Margirier et al. https://doi.org/10.5281/zenodo.10906772

Rowan, A. V. (2024b). Annvrowan/isosia: iSOSIA version used in Margirier et al. [Software]. *Zenodo*. https://doi.org/10.5281/zenodo.10959201

Rowan, A. V., Egholm, D. L., Quincey, D. J., & Glasser, N. F. (2015). Modelling the feedbacks between mass balance, ice flow and debris transport to predict the response to climate change of debris-covered glaciers in the Himalaya. *Earth and Planetary Science Letters*, *430*, 427–438. https://doi.org/10.1016/j.epsl.2015.09.004

Rowan, A. V., Egholm, D. L., Quincey, D. J., Hubbard, B., King, O., Miles, E. S., et al. (2021). The role of differential ablation and dynamic detachment in driving accelerating mass loss from a debris-covered Himalayan glacier. *Journal of Geophysical Research: Earth Surface*, *126*(9), e2020JF005761. https://doi.org/10.1029/2020JF005761

Sarr, A.-C., Mugnier, J.-L., Abrahami, R., Carcaillet, J., & Ravanel, L. (2019). Sidewall erosion: Insights from *in situ* -produced [10]Be concentrations measured on supraglacial clasts (Mont Blanc massif, France). *Earth Surface Processes and Landforms*, *44*, 1930–1944. https://doi.org/10.1002/esp.4620

Scherler, D. (2014). Climatic limits to headwall retreat in the Khumbu Himalaya, eastern Nepal. *Geology*, *42*(11), 1019–1022. https://doi.org/10.1130/G35975.1

Scherler, D., & Egholm, D. L. (2020). Production and transport of supraglacial debris: Insights from cosmogenic [10]Be and numerical modeling, Chhota Shigri Glacier, Indian Himalaya. *Journal of Geophysical Research: Earth Surface*, *125*. https://doi.org/10.1029/2020JF005586

Scherler, D., Wulf, H., & Gorelick, N. (2018). Global assessment of supraglacial debris-cover extents. *Geophysical Research Letters*, *45*(21), 11798–11805. https://doi.org/10.1029/2018GL080158

Serra, E., Mueller, D., Gegg, L., Firla, G., Piccoli, F., Hergarten, S., et al. (2025). Combined single grain and cobble luminescence dating of poorly bleached glaciofluvial deposits from the Swiss Alpine foreland. *Quaternary Geochronology*, *87*, 101650. https://doi.org/10.1016/j.quageo.2025.101650

Smiraglia, C., Diolaiuti, G., Casati, D., & Kirkbride, M. P. (2000). Recent areal and altinietric variations of Miage Glacier (Monte Bianco massif, Italian Alps) (p. 7).

Sohbati, R., Liu, J., Jain, M., Murray, A., Egholm, D., Paris, R., & Guralnik, B. (2018). Centennial-to millennial-scale hard rock erosion rates deduced from luminescence-depth profiles. *Earth and Planetary Science Letters*, *493*, 218–230. https://doi.org/10.1016/j.epsl.2018.04.017

Sohbati, R., Murray, A. S., Jain, M., Buylaert, J. P., & Thomsen, K. J. (2011). Investigating the resetting of OSL signals in rock surfaces. *Geochronometria*, *38*(3), 249–258. https://doi.org/10.2478/s13386-011-0029-2

Souza, P. E., Sohbati, R., Murray, A. S., Kroon, A., Clemmensen, L. B., Hede, M. U., & Nielsen, L. (2019). Luminescence dating of buried cobble surfaces from sandy beach ridges: A case study from Denmark. *Boreas*, *48*(4), 841–855. https://doi.org/10.1111/bor.12402

Stefaniak, A. M., Robson, B. A., Cook, S. J., Clutterbuck, B., Midgley, N. G., & Labadz, J. C. (2021). Mass balance and surface evolution of the debris-covered Miage Glacier, 1990–2018. *Geomorphology*, *373*, 107474. https://doi.org/10.1016/j.geomorph.2020.107474

Sun, C., Xie, B., Wang, R., Deng, X., & Wu, J. (2023). Investigation of internal damage evolution in gneiss considering water softening. *Scientific Reports*, *13*(1), 12672. https://doi.org/10.1038/s41598-023-39664-8

Thomson, M. H., Kirkbride, M. P., & Brock, B. W. (2000). *Twentieth century surface elevation change of the Miage Glacier, Italian Alps* (p. 7). IAHS-AISH publication.

Vincent, C., Gilbert, A., Jourdain, B., Piard, L., Ginot, P., Mikhalenko, V., et al. (2020). Strong changes in englacial temperatures despite insignificant changes in ice thickness at Dôme du Goûter glacier (Mont Blanc area). *The Cryosphere*, *14*(3), 925–934. https://doi.org/10.5194/tc-14-925-2020

Vincent, C., Le Meur, E., Six, D., & Funk, M. (2005). Solving the paradox of the end of the little ice age in the Alps. *Geophysical Research Letters*, *32*(9), 2005GL022552. https://doi.org/10.1029/2005GL022552

Wijngaard, R. R., Steiner, J. F., Kraaijenbrink, P. D., Klug, C., Adhikari, S., Banerjee, A., et al. (2019). Modeling the response of the langtang glacier and the hintereisferner to a changing climate since the little ice age. *Frontiers in Earth Science*, *7*, 143. https://doi.org/10.3389/feart.2019.00143

Zekollari, H., Fürst, J. J., & Huybrechts, P. (2014). Modelling the evolution of Vadret da Morteratsch, Switzerland, since the Little Ice Age and into the future. *Journal of Glaciology*, *60*(224), 1155–1168. https://doi.org/10.3189/2014JoG14J053

Zekollari, H., Huss, M., Farinotti, D., & Lhermitte, S. (2022). Ice-dynamical glacier evolution modeling—A review. *Reviews of Geophysics*, *60*(2). https://doi.org/10.1029/2021RG000754

Zhang, J., Tsukamoto, S., Nottebaum, V., Lehmkuhl, F., & Frechen, M. (2015). D_e plateau and its implications for post-IR IRSL dating of polymineral fine grains. *Quaternary Geochronology*, *30*, 147–153. https://doi.org/10.1016/j.quageo.2015.02.003